PHYSICAL REVIEW E **103**, 043304 (2021)

Lattice Boltzmann model for conjugate heat transfer across thin walls

David Korba and Like Li[*]

Department of Mechanical Engineering, Mississippi State University, Mississippi State, Mississippi 39762, USA

(Received 7 January 2021; accepted 22 March 2021; published 12 April 2021)

A lattice Boltzmann (LB) model with an efficient and accurate interface treatment for conjugate heat transfer across a thin wall between two different media is developed. The proposed interface treatment avoids fine meshing and computation within the thin layer; instead, the energy balance within the thin layer and the conjugate conditions on each interface are utilized to construct explicit updating schemes for the microscopic distribution functions of the LB model at the interior lattice nodes of the two media next to the thin layer. The proposed interface schemes reduce to the standard interface scheme for conjugate conditions in the literature in the limit of zero thickness of the thin layer, and thus it can be considered a more general interface treatment. A simplified version of the interface treatment is also proposed when the heat flux variation along the tangential direction of the thin layer is negligible. Three representative numerical tests are conducted to verify the applicability and accuracy of the proposed interface schemes. The results demonstrate that the intrinsic second-order accuracy of the LB model is preserved with the proposed interface schemes for thin layers with constant tangential fluxes, while for general situations with varying tangential fluxes, first-order accuracy is obtained. This interface treatment within the LB framework is attractive in conjugate heat transfer modeling involving thin layers for its simplicity, accuracy, and significant reduction in computational resources.

DOI: 10.1103/PhysRevE.103.043304

I. INTRODUCTION

The process of heat transfer between two media separated by a thin layer is encountered in numerous scientific and engineering problems. Representative examples include design of different types of heat exchangers with heat transfer between countercurrent fluid streams or between a fluid and a moving packed bed or falling particles that are separated by thin walls [1–3], solar thermal receivers with modular absorbers of thin metallic or ceramic tubes [4–7], latent or thermochemical energy storage units where the porous media are heated (cooled) by an external hot (cold) fluid going through a thin-walled channel [8–11], heat pipes with insulation layers [12,13], and heat conduction in multilayer composite materials [14], just to name a few. Thermal transport in those systems are essentially conjugate heat transfer problems due to the different thermophysical and transport properties of the adjacent materials. Modeling of the conjugate heat transfer across the thin layer is a challenging task as the conjugate conditions need to be satisfied on each side of the thin layer and its dimension can be orders of magnitude smaller than the adjacent media, which would typically require nonuniform or adaptive meshing.

The lattice Boltzmann method (LBM) has become an alternative and attractive numerical method for heat and mass transfer in the last decade [15–18]. In addition to the inherited benefits of the LBM for fluid flow—ease of implementation, convenience in boundary treatment involving complex geometry, and the ability to be performed as a parallel computation leading to greatly reduced computational demand—the LBM is particularly attractive for heat and mass transfer simulations due to the fact that the boundary and interfacial macroscopic variables of interest [e.g., Dirichlet-type boundary temperature (concentration), Neumann-type boundary heat and mass fluxes, and interfacial temperature (concentration) and their fluxes] can be directly related to the microscopic distribution functions (DFs) in the LBM so that those physical boundary and conjugate conditions can be directly implemented or satisfied to the intrinsic second-order accuracy [15,19–21]. Therefore, extensive interest and effort have been devoted in the literature to develop effective and accurate interface schemes in the LBM for conjugate heat and mass transfer problems (see Refs. [22–27] and references therein). While those interface schemes are directly applicable to the above-mentioned conjugate heat transfer across thin walls, they would require either very fine mesh in the whole computational domain in order to resolve the thin layer when using the standard uniform mesh in the Cartesian coordinates, or nonuniform meshing in the thin layer and the other domains. For the latter, although various grid-refinement, grid-stretching, and multiblock techniques have been proposed and verified in the LBM for fluid flow and heat and mass transfer [28–33], they require additional treatment of the DFs and matching of the relaxation time coefficients in the LBM in the regions near the interfaces, typically along with the necessity of data interpolation and transfer between the adjacent domains. An effective interface treatment in the LBM framework for conjugate heat transfer across a thin layer using the standard Cartesian uniform mesh and with acceptable grid resolution is thus desired.

This paper aims to develop and verify a convenient and accurate interface treatment in the LB model for conjugate

---

[*] likeli@me.msstate.edu

heat transfer across thin layers without mesh allocation or LBM computation within the thin layer. The conjugate conditions on both sides of the thin layer are satisfied through an energy balance analysis in the control volume enclosing the sandwiched layer, and those relations are implemented to develop explicit updating schemes for the DFs next to the thin layer to complete the standard "collision-streaming" process in the LBM nodes within the two media of major interest. The applicability and accuracy of the proposed interface schemes are verified through three representative numerical tests for which analytical solutions are available.

The remainder of this paper is structured as follows. First, the LB models for the scalar convection-diffusion equation (CDE) in the Cartesian coordinate and the axisymmetric CDE in the cylindrical coordinate systems are reviewed in Secs. II and III, respectively, followed by a presentation of the specific schemes for thermal boundary conditions and the standard conjugate conditions for zero-thickness interfaces in Sec. IV. Next, our proposed schemes for thin-layered interfaces are detailed in Sec. V considering three different scenarios. Section VI presents a detailed numerical verification and accuracy analysis of the proposed schemes with three test cases. Conclusions are given in Sec. VII. The Appendix illustrates the analytical solutions to the test cases in Secs. VI A and VI C.

II. LATTICE BOLTZMANN MODEL FOR THE STANDARD CONVECTION-DIFFUSION EQUATION

The general convection-diffusion equation with source terms for heat and mass transfer can be written as

$$\frac{\partial \phi}{\partial t} + \nabla \cdot (\mathbf{u}\phi) = \nabla \cdot (D_{ij}\nabla\phi) + G, \tag{1}$$

where ϕ is the dimensionless macroscopic variable of interest such as normalized temperature or concentration, t the time, $\mathbf{u}$ the velocity vector, D_{ij} the diffusion coefficient, and G represents any combination of source terms.

In the LB method, the following evolution equation is proposed to model and recover the CDE (1) [15,18]:

$$\begin{aligned} g_\alpha(\mathbf{x}+\mathbf{e}_\alpha\delta t, t+\delta t) - g_\alpha(\mathbf{x}, t) \\ = [\mathbf{L}\cdot(\mathbf{g}-\mathbf{g}^{\mathrm{eq}})(\mathbf{x}, t)]_\alpha + \omega_\alpha G(\mathbf{x}, t)\delta t, \end{aligned} \tag{2}$$

where the microscopic distribution function, $g_\alpha(\mathbf{x}, t) \equiv g(\mathbf{x}, \boldsymbol{\xi}_\alpha, t)$, is defined in the discrete velocity space, $\boldsymbol{\xi}$ is the particle velocity vector that is discretized to a small set of discrete velocities $\{\boldsymbol{\xi}_\alpha | \alpha = 0, 1, \ldots, m-1\}$, $\mathbf{e}_\alpha$ the αth discrete velocity vector, δt the time step, $\mathbf{L}$ the collision operator, $g_\alpha^{\mathrm{eq}}(\mathbf{x}, t)$ the equilibrium distribution function, and ω_α the weight coefficient. The macroscopic scalar variable is obtained from

$$\phi(\mathbf{x}, t) = \sum_{\alpha=0}^{m-1} g_\alpha(\mathbf{x}, t), \tag{3}$$

and the equilibrium DF can be expressed as [15,18]

$$g_\alpha^{\mathrm{eq}} = \omega_\alpha \phi \left(1 + \frac{\mathbf{e}_\alpha \cdot \mathbf{u}}{c_s^2}\right). \tag{4}$$

Regarding the collision operator $\mathbf{L}$, there are three models that have been extensively studied, including the earliest and most original Bhatnagar-Gross-Krook (BGK) (also commonly referred to as the single relaxation-time model) [34], the two relaxation-time model [35], and the general multiple relaxation-time (MRT) model [15,18]. In addition, different lattice structures have also been examined with applications in various situations (e.g., see Refs. [18,36]). In this work, the D2Q5 MRT LB model originally proposed by Yoshida and Nagaoka [15], which is attractive due to its simple implementation and second-order accuracy, is used. Specifically, a transformation matrix $\mathbf{M}$ is defined to map the DFs to their moment space: $\mathbf{m} = \mathbf{M}\cdot\mathbf{g}$ and $\mathbf{m}^{\mathrm{eq}} = \mathbf{M}\cdot\mathbf{g}^{\mathrm{eq}}$, and the collision operator becomes

$$\begin{aligned} [\mathbf{L}\cdot(\mathbf{g}-\mathbf{g}^{\mathrm{eq}})]_\alpha &= -[\mathbf{M}^{-1}\mathbf{S}\mathbf{M}\cdot(\mathbf{g}-\mathbf{g}^{\mathrm{eq}})]_\alpha \\ &= -[\mathbf{M}^{-1}\mathbf{S}\cdot(\mathbf{m}-\mathbf{m}^{\mathrm{eq}})]_\alpha, \end{aligned} \tag{5}$$

where $\mathbf{S}$ is a matrix of relaxation-time coefficients, τ_{ij}, which are related to the diffusion coefficients D_{ij} as in the following:

$$\tau_{ij} = \frac{1}{2}\delta_{ij} + \frac{\delta t}{\varepsilon_D \delta x^2} D_{ij}, \tag{6}$$

in order to recover the CDE. The constant coefficient $\varepsilon_D = 1/3$ and the equilibrium moments can be explicitly derived as [18,19,22]

$$\mathbf{m}^{\mathrm{eq}} = [\phi, u\phi, v\phi, 2\phi/3, 0]^{\mathrm{T}}. \tag{7}$$

The standard "collision-streaming" procedure is also used in this work for efficient computational implementation, with *collision step:*

$$\begin{aligned} \hat{g}_\alpha(\mathbf{x}, t) = g_\alpha(\mathbf{x}, t) - [\mathbf{M}^{-1}\mathbf{S}\cdot(\mathbf{m}-\mathbf{m}^{\mathrm{eq}})(\mathbf{x}, t)]_\alpha \\ + \omega_\alpha G(\mathbf{x}, t)\delta t, \text{ and} \end{aligned} \tag{8}$$

streaming step:

$$g_\alpha(\mathbf{x}+\mathbf{e}_\alpha\delta t, t+\delta t) = \hat{g}_\alpha(\mathbf{x}, t), \tag{9}$$

where $\hat{g}_\alpha$ represents the postcollision state.

III. LATTICE BOLTZMANN MODEL FOR THE AXISYMMETRIC CONVECTION-DIFFUSION EQUATION

For the wide range of engineering applications involving conjugate heat transfer between different fluids or a fluid and a porous bed separated by an annular medium, such as heat exchangers, tubular solar collectors (reactors), etc., the heat transfer process is axisymmetric, and thus axisymmetric lattice Boltzmann models, as discussed by multiple authors [37–40], can be very advantageous. In this work, we apply the D2Q5 MRT axisymmetric model proposed by Li *et al.* [37]. The typical axisymmetric CDE can be described as

$$\begin{aligned} \frac{\partial\phi}{\partial t} + \frac{\partial}{r\partial r}(ru_r\phi) + \frac{\partial}{\partial z}(u_z\phi) \\ = \frac{\partial}{r\partial r}\left(rD_{rr}\frac{\partial\phi}{\partial r}\right) + \frac{\partial}{\partial z}\left(D_{zz}\frac{\partial\phi}{\partial z}\right) + G, \end{aligned} \tag{10}$$

where r and z represent the radial and axial directions, respectively, D_{rr} and D_{zz} are the diagonal diffusion coefficients of the tensor D_{ij}, and u_r and u_z are the respective velocity components. The proposed model effectively rearranges this equation to fit the form shown in Eq. (1) as

$$\frac{\partial \phi}{\partial t} + \frac{\partial}{\partial r}(u_r \phi) + \frac{\partial}{\partial z}(u_z \phi) = \frac{\partial}{\partial r}\left(D_{rr}\frac{\partial \phi}{\partial r}\right) + \frac{\partial}{\partial z}\left(D_{zz}\frac{\partial \phi}{\partial z}\right) + S_{a1} + S_{a2} + G, \quad (11)$$

with $S_{a1} = -\frac{u_r \phi}{r}$, $S_{a2} = \frac{D_{rr}}{r}\frac{\partial \phi}{\partial r}$, which are now in terms of the pseudo-Cartesian coordinate system with two additional source components. For the above CDE, the MRT evolution equation for the DFs is thus redefined as

$$\begin{aligned} g_\alpha(\mathbf{x} + \mathbf{e}_\alpha \delta t, t + \delta t) - g_\alpha(\mathbf{x}, t) &= [\mathbf{L} \cdot (\mathbf{g} - \mathbf{g}^{\text{eq}})(\mathbf{x}, t)]_\alpha + \omega_\alpha [S_{a1}(\mathbf{x}, t) \\ &\quad + S_{a2}(\mathbf{x}, t) + G(\mathbf{x}, t)]\delta t, \end{aligned} \quad (12)$$

where $[\mathbf{L} \cdot (\mathbf{g} - \mathbf{g}^{\text{eq}})(\mathbf{x}, t)]_\alpha$ takes the form as described in Eq. (5). The leading-order solution of the CDE can be obtained from Eq. (3). The additional source terms can be described in terms of the DFs as

$$S_{a1} = -\frac{u_r \phi}{r} = -\frac{u_r}{r}\sum_{\alpha=0}^{m-1} g_\alpha(\mathbf{x}, t) = -\frac{u_r}{r}\sum_{\alpha=0}^{m-1} g_\alpha^{\text{eq}}(\mathbf{x}, t) \quad (13)$$

and

$$\begin{aligned} S_{a2} = \frac{D_{rr}}{r}\frac{\partial \phi}{\partial r} &= -\frac{1}{r}\left(1 - \frac{1}{2\tau_{rr}}\right)\frac{\delta x}{\delta t}\sum_{\alpha=0}^{m-1} e_{\alpha r} g_\alpha^{\text{neq}} \\ &= -\frac{1}{r}\left(1 - \frac{1}{2\tau_{rr}}\right)\frac{\delta x}{\delta t}\sum_{\alpha=0}^{m-1} e_{\alpha r}[g_\alpha - g_\alpha^{\text{eq}}]. \end{aligned} \quad (14)$$

The reader is referred to Refs. [37–41] for further discussion on the axisymmetric model and associated comparisons of accuracy behavior.

IV. THERMAL BOUNDARY CONDITIONS AND STANDARD CONJUGATE CONDITIONS

For both Dirichlet and Neumann-type thermal boundary conditions, second-order accurate boundary treatments based on the interpolation of postcollision distribution functions were proposed and verified in Ref. [19]. By treating the interface as a zero-thickness shared boundary, those boundary schemes were applied to relate the interfacial scalar values and their fluxes to the DFs at the lattice nodes next to the interface for conjugate conditions. In this work, we make use of those relationships on each side of the thin wall and construct convenient interface schemes. For completeness, the boundary and interface schemes are summarized below and the derivation of the specific thin-wall conjugate condition schemes will be provided in the next section.

For the Dirichlet boundary condition $\phi_w = \Phi_d$, the following was proposed [19]:

$$\begin{aligned} g_{\bar{\alpha}}(\mathbf{x}_f, t + \delta t) &= c_{d1}\hat{g}_\alpha(\mathbf{x}_f, t) + c_{d2}\hat{g}_\alpha(\mathbf{x}_{ff}, t) \\ &\quad + c_{d3}\hat{g}_{\bar{\alpha}}(\mathbf{x}_f, t) + c_{d4}\varepsilon_D \Phi_d, \end{aligned} \quad (15)$$

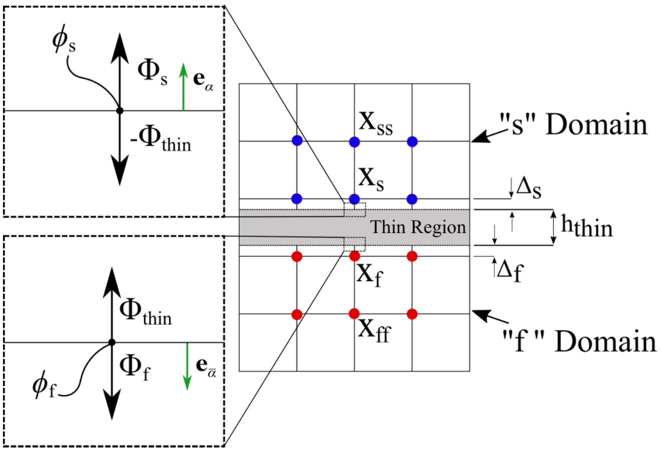

FIG. 1. Domain setup and layout of lattice nodes for conjugate heat transfer across a flat, thin plate.

and the Neumann boundary scheme can be written as

$$\begin{aligned} g_{\bar{\alpha}}(\mathbf{x}_f, t + \delta t) &= c_{n1}\hat{g}_\alpha(\mathbf{x}_f, t) + c_{n2}\hat{g}_\alpha(\mathbf{x}_{ff}, t) \\ &\quad + c_{n3}\hat{g}_{\bar{\alpha}}(\mathbf{x}_f, t) + c_{n4}(\delta t/\delta x)\Phi_{n\bar{\alpha}}, \end{aligned} \quad (16)$$

where $\mathbf{e}_{\bar{\alpha}} = -\mathbf{e}_\alpha$ pointing from the boundary node to the interior lattice nodes $\mathbf{x}_f$ and $\mathbf{x}_{ff}$(see Fig. 1), the coefficients c_{di} and c_{ni} ($i = 1, 2, 3,$ and 4) are only related to the local lattice link fraction Δ, and $\Phi_{n\bar{\alpha}} = D\partial\phi/\partial x|_{\mathbf{e}_{\bar{\alpha}}}$ is the boundary flux in the lattice velocity vector $\mathbf{e}_{\bar{\alpha}}$ direction [19].

Specifically, Li *et al.* [19] proposed three particular schemes based on an adjustable parameter, c_{d1}, for the Dirichlet scheme which are determined with

$$\text{Scheme 1: } c_{d1} = \begin{cases} -2\Delta, (0 \leqslant \Delta \leqslant 0.5), \\ -1/2\Delta, (\Delta > 0.5), \end{cases} \quad (17a)$$

$$\text{Scheme 2: } c_{d1} = -2(1 - \Delta), \quad \text{and,} \quad (17b)$$

$$\text{Scheme 3: } c_{d1} = -1, \quad (17c)$$

with the other coefficients thus related to the parameter as

$$c_{d2} = -\frac{2\Delta c_{d1} + 1}{2\Delta + 1}, \quad c_{d3} = \frac{c_{d1} + 2\Delta}{2\Delta + 1},$$

$$\text{and} \quad c_{d4} = \frac{-c_{d1} + 1}{2\Delta + 1}. \quad (18)$$

For the results presented in this work, Scheme 2 will be utilized and previous accuracy analysis [18,19,22,27] has shown accurate results with the other schemes. For the Neumann scheme, the coefficients can be uniquely determined to preserve the second-order accuracy as

$$c_{n1} = 1, \; c_{n2} = -\frac{2\Delta - 1}{2\Delta + 1},$$

$$c_{n3} = \frac{2\Delta - 1}{2\Delta + 1}, \quad \text{and} \quad c_{n4} = \frac{2}{2\Delta + 1}. \quad (19)$$

The conjugate interface conditions can be expressed in general formulation as [27]

$$\phi_f = \phi_s + \phi_{\text{jump}}, \quad \text{and} \quad (20)$$

$$\mathbf{n}\cdot(k\nabla\phi+\rho c_p\mathbf{u}\phi)_f=\mathbf{n}\cdot(k\nabla\phi+\rho c_p\mathbf{u}\phi)_s+\mathbf{n}\cdot\mathbf{q}^T_{\text{jump}},\quad\text{for heat transfer, or}\tag{21a}$$

$$\mathbf{n}\cdot(D_m\nabla\phi+\mathbf{u}\phi)_f=\mathbf{n}\cdot(D_m\nabla\phi+\mathbf{u}\phi)_s+\mathbf{n}\cdot\mathbf{q}^C_{\text{jump}},\quad\text{for mass transfer,}\tag{21b}$$

where k is the thermal conductivity of the materials, ρ the density, c_p the specific heat, and ϕ_{jump} and $\mathbf{q}_{\text{jump}}$ the possible scalar and flux jump conditions at the interface. The subscripts f and s refer to the conterminous domains sharing a common boundary, typically referred to as the *fluid-solid* adjacent boundaries, and $\mathbf{n}$ represents the unit normal vector. For simplified situations when the velocity component normal to the interface is zero and no jump conditions are present, Eqs. (20) and (21) reduce to

$$\phi_f=\phi_s,\tag{22}$$

$$\mathbf{n}\cdot(D\nabla\phi)_f=\sigma\mathbf{n}\cdot(D\nabla\phi)_s,\tag{23}$$

where $D=\frac{k}{\rho c_p}$, $\sigma=\frac{(\rho c_p)_s}{(\rho c_p)_f}$ in heat transfer and $D=D_m$, $\sigma=1$ in mass transfer.

The interface for conjugate conditions can be considered as a shared boundary for the adjacent domains; thus, the following are noted based on the Dirichlet scheme:

$$\begin{aligned}g_{\bar{\alpha}}(\mathbf{x}_f,t+\delta t)=&\,c_{d1}\hat{g}_\alpha(\mathbf{x}_f,t)+c_{d2}\hat{g}_\alpha(\mathbf{x}_{ff},t)\\&+c_{d3}\hat{g}_{\bar{\alpha}}(\mathbf{x}_f,t)+c_{d4}\varepsilon_D\Phi_{df},\ \text{in domain 1,}\end{aligned}\tag{24a}$$

$$\begin{aligned}g_\alpha(\mathbf{x}_s,t+\delta t)=&\,c^*_{d1}\hat{g}_{\bar{\alpha}}(\mathbf{x}_s,t)+c^*_{d2}\hat{g}_{\bar{\alpha}}(\mathbf{x}_{ss},t)\\&+c^*_{d3}\hat{g}_\alpha(\mathbf{x}_s,t)+c^*_{d4}\varepsilon_D\Phi_{ds},\ \text{in domain 2,}\end{aligned}\tag{24b}$$

and the Neumann scheme yields

$$\begin{aligned}&g_{\bar{\alpha}}(\mathbf{x}_f,t+\delta t)\\&\quad=c_{n1}\hat{g}_\alpha(\mathbf{x}_f,t)+c_{n2}\hat{g}_\alpha(\mathbf{x}_{ff},t)\\&\qquad+c_{n3}\hat{g}_{\bar{\alpha}}(\mathbf{x}_f,t)+c_{n4}(\delta t/\delta x)\Phi_{n\bar{\alpha}},\ \text{in domain 1,}\end{aligned}\tag{25a}$$

$$\begin{aligned}&g_\alpha(\mathbf{x}_s,t+\delta t)\\&\quad=c^*_{n1}\hat{g}_{\bar{\alpha}}(\mathbf{x}_s,t)+c^*_{n2}\hat{g}_{\bar{\alpha}}(\mathbf{x}_{ss},t)\\&\qquad+c^*_{n3}\hat{g}_\alpha(\mathbf{x}_s,t)+c^*_{n4}(\delta t/\delta x)\Phi_{n\alpha},\ \text{in domain 2,}\end{aligned}\tag{25b}$$

where $\Phi_{df}=\Phi_{ds}$ are the interface scalar temperature and $\Phi_{n\alpha}=-\Phi_{n\bar{\alpha}}$ are the interfacial fluxes, both of which can be conveniently evaluated within the LB framework; the coefficients c^*_{di} and $c^*_{ni}(i=1,2,3,\text{ and }4)$ are related to c_{di} and c_{ni} as $c^*_{di}=c_{di}(\Delta^*)=c_{di}(1-\Delta)$, and $c^*_{ni}=c_{ni}(\Delta^*)=c_{ni}(1-\Delta)$.

Combining Eqs. (20), (21), (24), and (25), one can obtain a system of equations to analytically solve for the DFs $g_{\bar{\alpha}}(\mathbf{x}_f,t+\delta t)$ and $g_\alpha(\mathbf{x}_s,t+\delta t)$. Note that Eqs. (22)–(25) are used in the formulations presented in this paper. For brevity, here we present the following interface scheme for decoupled conjugate conditions (i.e., when the lattice vectors $\mathbf{e}_{\bar{\alpha}}$ and $\mathbf{e}_\alpha$ are aligned with the normal $\mathbf{n}$ of the interface) [22]:

$$\begin{aligned}g_{\bar{\alpha}}(\mathbf{x}_f,t+\delta t)=&\,A^f_1\hat{g}_\alpha(\mathbf{x}_f,t)+A^f_2\hat{g}_\alpha(\mathbf{x}_{ff},t)+A^f_3\hat{g}_{\bar{\alpha}}(\mathbf{x}_f,t)\\&+B^f_1\hat{g}_{\bar{\alpha}}(\mathbf{x}_s,t)+B^f_2\hat{g}_{\bar{\alpha}}(\mathbf{x}_{ss},t)+B^f_3\hat{g}_\alpha(\mathbf{x}_s,t),\end{aligned}\tag{26a}$$

$$\begin{aligned}g_\alpha(\mathbf{x}_s,t+\delta t)=&\,A^s_1\hat{g}_{\bar{\alpha}}(\mathbf{x}_s,t)+A^s_2\hat{g}_{\bar{\alpha}}(\mathbf{x}_{ss},t)+A^s_3\hat{g}_\alpha(\mathbf{x}_s,t)\\&+B^s_1\hat{g}_\alpha(\mathbf{x}_f,t)+B^s_2\hat{g}_\alpha(\mathbf{x}_{ff},t)+B^s_3\hat{g}_{\bar{\alpha}}(\mathbf{x}_f,t),\end{aligned}\tag{26b}$$

with

$$\left.\begin{aligned}A^f_i&=\left(\frac{\sigma c_{di}}{c_{d4}c^*_{n4}}+\frac{c_{ni}}{c^*_{d4}c_{n4}}\right)\Big/P\\B^f_i&=\sigma\left(\frac{c^*_{ni}-c^*_{di}}{c^*_{d4}c^*_{n4}}\right)\Big/P\\A^s_i&=\left(\frac{c^*_{di}}{c^*_{d4}c_{n4}}+\frac{\sigma c^*_{ni}}{c_{d4}c^*_{n4}}\right)\Big/P\\B^s_i&=\left(\frac{c_{ni}-c_{di}}{c_{d4}c_{n4}}\right)\Big/P\end{aligned}\right\},\quad(i=1,2,3),\tag{27a}$$

and

$$P=\frac{\sigma}{c_{d4}c^*_{n4}}+\frac{1}{c^*_{d4}c_{n4}}.\tag{27b}$$

V. CONJUGATE CONDITIONS ACROSS THIN WALLS

In this section, convenient and accurate LB schemes are derived to satisfy the conjugate conditions across a thin region sandwiched between two domains of major interest. The main attractiveness of the proposed treatment is that it does not require additional meshing, node distribution, or numerical computation within the thin layer; instead, the energy balance within and the conjugate conditions on both sides of the thin layer are utilized to construct suitable schemes to complete the streaming step [see Eq. (9)] for the DFs at the lattice nodes next to the thin layer. Specifically, we consider three basic scenarios representing different configurations and applications. The first two setups are selected to show the treatments for thin flat plates and annular layers, for which the standard and axisymmetric LB models in Secs. II and III are implemented, respectively. In addition, the heat flux in the tangential direction is assumed to be zero or constant so that the heat flow rates in the normal direction on both sides of the thin layer are balanced in those two cases, while the third setup is for the general situation with varying normal and tangential fluxes. For brevity, only steady cases are considered and the scalar and flux jumps at both interfaces for all cases are assumed to be zero. A similar approach can be used to develop a scheme to resolve the transient variations, using information from the past time steps, such as an additional discretization of the transient term with the Euler method.

A. Conjugate heat transfer through flat, thin layer with constant tangential flux

The thin-layered setup is shown in Fig. 1, where Φ refers to the normal heat fluxes at the interfaces of concern. The s and f subscripts refer to the upper and lower domains that are resolved with the LBM, and the *thin* subscript denotes the sandwiched middle layer.

Assuming zero normal velocity, the normal heat fluxes at the two interfaces in Fig. 1 can be related to that through the thin layer as

$$\Phi_f = -D_f\frac{\partial\phi_f}{\partial n_f} = -\sigma_{f,\text{thin}}\Phi_{\text{thin}} = \sigma_{f,\text{thin}}D_{\text{thin}}\frac{\partial\phi_{\text{thin}}}{\partial n_{\text{thin}}} \tag{28a}$$

and

$$\Phi_s = -D_s\frac{\partial\phi_s}{\partial n_s} = \sigma_{s,\text{thin}}\Phi_{\text{thin}} = -\sigma_{s,\text{thin}}D_{\text{thin}}\frac{\partial\phi_{\text{thin}}}{\partial n_{\text{thin}}}, \tag{28b}$$

where

$$\sigma_{f,\text{thin}} = \frac{(\rho c_p)_{\text{thin}}}{(\rho c_p)_f} \quad \text{and} \quad \sigma_{s,\text{thin}} = \frac{(\rho c_p)_{\text{thin}}}{(\rho c_p)_s}. \tag{28c}$$

Note that while we use the "fluid" and "solid" notations for consistency with previous papers, both domains can be fluidic or solid as will later be demonstrated.

The combination of Eqs. (28a), (28b) would yield

$$\Phi_f = -\frac{\sigma_{f,\text{thin}}}{\sigma_{s,\text{thin}}}\Phi_s = -\frac{(\rho c_p)_s}{(\rho c_p)_f}\Phi_s. \tag{29}$$

The above can also be directly obtained from the overall energy balance through the thin layer.

Also, with the assumption that the heat flow rate in the tangential direction of the thin layer is constant, the heat flow rate in the normal direction would be constant for steady cases. It is pointed out that the "thin-wall" assumption refers to cases where the heat flow rate is constant (or has little deviation) in the normal direction of the sandwiched layer. This condition can be exhibited for thicker walls; however, for such cases, a more direct approach is to allocate lattice nodes within the middle layer and implement the standard conjugate interface scheme on both sides of that layer. Furthermore, integration of the heat flow rate over the entire thin layer yields

$$\Phi_{\text{thin}} = -\frac{k_{\text{thin}}}{(\rho c_p)_{\text{thin}}}\frac{\phi_s - \phi_f}{h_{\text{thin}}} = -D_{\text{thin}}\frac{\phi_s - \phi_f}{h_{\text{thin}}}. \tag{30}$$

Substitution of Eq. (30) into (28a), (28b) gives

$$\Phi_f = \sigma_{f,\text{thin}}D_{\text{thin}}\frac{\phi_s - \phi_f}{h_{\text{thin}}} \tag{31a}$$

and

$$\Phi_s = -\sigma_{s,\text{thin}}D_{\text{thin}}\frac{\phi_s - \phi_f}{h_{\text{thin}}}. \tag{31b}$$

Clearly, the relationships in Eqs. (29) and (31a), (31b) now constitute two conjugate conditions for the temperature and flux components ϕ_f, ϕ_s, Φ_f, and Φ_s similar to the standard conjugate conditions for a zero-thickness interface in Eqs. (22), (23). Following the derivation of the interface schemes in the previous section, we propose similar interface schemes for conjugate heat transfer through thin walls as in Eqs. (26a), (26b), now with the new coefficients

$$\left.\begin{aligned}
A_i^f &= \left(\frac{\varepsilon_D h_{\text{thin}}}{c_{n4}c_{n4}^*} + \frac{Q}{c_{d4}^*c_{n4}}\right)\frac{c_{ni}}{P} + \left(\frac{\sigma Q}{c_{d4}c_{n4}^*}\right)\frac{c_{di}}{P}\\
B_i^f &= \left(\frac{\sigma Q}{c_{d4}^*c_{n4}^*}\right)\frac{(c_{ni}^* - c_{di}^*)}{P}\\
A_i^s &= \left(\frac{\varepsilon_D h_{\text{thin}}}{c_{n4}c_{n4}^*} + \frac{\sigma Q}{c_{d4}c_{n4}^*}\right)\frac{c_{ni}^*}{P} + \left(\frac{Q}{c_{d4}^*c_{n4}}\right)\frac{c_{di}^*}{P}\\
B_i^s &= \left(\frac{Q}{c_{d4}c_{n4}}\right)\frac{(c_{ni} - c_{di})}{P}
\end{aligned}\right\} \quad (i = 1, 2, 3), \tag{32a}$$

where

$$Q = \sigma_{s,\text{thin}}D_{\text{thin}}\frac{\delta t}{\delta x}, \;\; P = \frac{\varepsilon_D h_{\text{thin}}}{c_{n4}c_{n4}^*} + \frac{Q}{c_{d4}^*c_{n4}} + \frac{\sigma Q}{c_{d4}c_{n4}^*}, \tag{32b}$$

and $c_{di} = c_{di}(\Delta_f)$, $c_{ni} = c_{ni}(\Delta_f)$, $c_{di}^* = c_{di}^*(\Delta_s) = c_{di}(1 - \Delta_s)$, $c_{ni}^* = c_{ni}^*(\Delta_s) = c_{ni}(1 - \Delta_s)$, $i = 1$–4, which directly allow for the unknown DFs $g_{\bar{\alpha}}(\mathbf{x}_f, t + \delta t)$ and $g_\alpha(\mathbf{x}_s, t + \delta t)$ to be obtained to complete the "streaming" step without the need for additional node allocation or LBM computation within the thin layer.

It is worth noting that in the limit of zero thickness ($h_{\text{thin}} = 0$), Eqs. (31a), (31b) would yield $\phi_f = \phi_s$, and the proposed scheme in Eqs. (32a), (32b) reduces to

$$\left.\begin{aligned}
A_i^f &= \left(\frac{\sigma c_{di}}{c_{d4}c_{n4}^*} + \frac{c_{ni}}{c_{d4}^*c_{n4}}\right)\Big/P\\
B_i^f &= \sigma\left(\frac{c_{ni}^* - c_{di}^*}{c_{d4}^*c_{n4}^*}\right)\Big/P\\
A_i^s &= \left(\frac{c_{di}^*}{c_{d4}^*c_{n4}} + \frac{\sigma c_{ni}^*}{c_{d4}c_{n4}^*}\right)\Big/P\\
B_i^s &= \left(\frac{c_{ni} - c_{di}}{c_{d4}c_{n4}}\right)\Big/P
\end{aligned}\right\} \quad (i = 1, 2, 3), \tag{33a}$$

with

$$P = \frac{\sigma}{c_{d4}c_{n4}^*} + \frac{1}{c_{d4}^*c_{n4}}. \tag{33b}$$

It is observed that the coefficients in Eqs. (33a), (33b) match exactly with those in Eqs. (27a), (27b). Thus, the present interface scheme is able to recover that for the standard conjugate conditions with zero-thickness interface.

As will later be discussed in Sec. VI A, Eqs. (26), (32) can be used to retain the innate second-order accurate LBM scheme for straight interfaces for all Δ values. However, it is also favorable to present a simplified case for $\Delta = 0.5$ for simple and efficient implementation. Assuming $\Delta_f = \Delta_s = 0.5$, Eqs. (26), (32) reduce to

$$\begin{aligned}
g_{\bar{\alpha}}(\mathbf{x}_f, t + \delta t) = {}& \frac{\varepsilon_D h_{\text{thin}} + (1 - \sigma)Q}{\varepsilon_D h_{\text{thin}} + (1 + \sigma)Q}\hat{g}_\alpha(\mathbf{x}_f, t)\\
&+ \frac{2\sigma Q}{\varepsilon_D h_{\text{thin}} + (1 + \sigma)Q}\hat{g}_{\bar{\alpha}}(\mathbf{x}_s, t),
\end{aligned} \tag{34a}$$

$$\begin{aligned}
g_\alpha(\mathbf{x}_s, t + \delta t) = {}& \frac{\varepsilon_D h_{\text{thin}} - (1 - \sigma)Q}{\varepsilon_D h_{\text{thin}} + (1 + \sigma)Q}\hat{g}_{\bar{\alpha}}(\mathbf{x}_s, t)\\
&+ \frac{2Q}{\varepsilon_D h_{\text{thin}} + (1 + \sigma)Q}\hat{g}_\alpha(\mathbf{x}_f, t).
\end{aligned} \tag{34b}$$

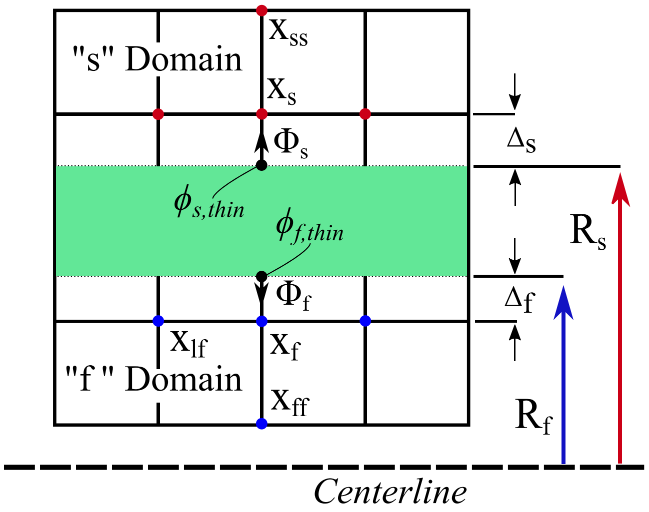

FIG. 2. Domain setup and layout of lattice nodes in the axisymmetric LB model for conjugate heat transfer across an annular thin medium.

Again, in the limit of $h_{\text{thin}} = 0$, it becomes

$$g_{\bar{\alpha}}(\mathbf{x}_f, t+\delta t) = \frac{1-\sigma}{1+\sigma}\hat{g}_{\alpha}(\mathbf{x}_f, t) + \frac{2\sigma}{1+\sigma}\hat{g}_{\bar{\alpha}}(\mathbf{x}_s, t), \tag{35a}$$

$$g_{\alpha}(\mathbf{x}_s, t+\delta t) = -\frac{1-\sigma}{1+\sigma}\hat{g}_{\bar{\alpha}}(\mathbf{x}_s, t) + \frac{2}{1+\sigma}\hat{g}_{\alpha}(\mathbf{x}_f, t). \tag{35b}$$

This is consistent with the decoupled conjugate scheme at $\Delta = 0.5$ originally proposed in Ref. [22].

The scheme in Eqs. (34a), (34b) is a convenient simplification for faster simulations and when it is undesirable to track the specific locations of the boundaries relative the LB grid, but it is stressed that second-order accuracy will only be achieved under the specific case of $\Delta = 0.5$ with an expected decreased convergence order for $\Delta \neq 0.5$ and curved geometry.

B. Conjugate heat transfer through annular thin layer with constant tangential flux

While the proposed model in Sec. V A can resolve the thin region in typical planar coordinates, it is also advantageous to present a model for cylindrical coordinates, since a common application that this framework can be applied to is the solution of the CDE for "thin-walled pipes." For the axisymmetric model, we present the domain schematic and lattice layout as shown in Fig. 2.

It should be noted that the fluxes at the two interfaces on each side of the thin region are not the same; rather, the heat flow rate is conserved. Thus, the fluxes can be directly related as before with an additional radius ratio as

$$k_f \frac{\partial \phi_f}{\partial n_f}\bigg|_{r=R_f} = \left(\frac{R_s}{R_f}\right) k_s \frac{\partial \phi_s}{\partial n_s}\bigg|_{r=R_s}, \tag{36}$$

which can be written in a form similar to Eq. (29) as

$$\Phi_s = -\left(\frac{R_f}{R_s}\right)\frac{\Phi_f}{\sigma_{f,\text{thin}}\sigma_{s,\text{thin}}}. \tag{37}$$

Similarly, assuming constant tangential flux along the interface, the normal heat flow rate is uniform throughout the thin layer; thus, the normal flux can be calculated with the temperatures at the interfaces as

$$R_f k_f \frac{\partial \phi_f}{\partial n_f}\bigg|_{r=R_f} = k_{\text{thin}} \frac{\phi_s - \phi_f}{\ln(R_s/R_f)}. \tag{38}$$

Now that two relations have been obtained relating the fluxes (Φ_f, Φ_s) and macroscopic variables (ϕ_f, ϕ_s), we can develop similar conjugate schemes as given in Eqs. (26a), (26b) with the new coefficients within the axisymmetric LB model:

$$\begin{aligned} A_i^f &= \left[\frac{\varepsilon_D R_f R_s \ln(R_s/R_f)}{c_{n4}c_{n4}^*} + \frac{R_f Q}{c_{d4}^* c_{n4}}\right]\frac{c_{ni}}{P} + \left(\frac{R_s \sigma Q}{c_{d4}c_{n4}^*}\right)\frac{c_{di}}{P} \\ B_i^f &= \left(\frac{R_s \sigma Q}{c_{d4}^* c_{n4}^*}\right)\frac{(c_{ni}^* - c_{di}^*)}{P} \\ A_1^s &= \left[\frac{\varepsilon_D R_f R_s \ln(R_s/R_f)}{c_{n4}c_{n4}^*} + \frac{R_s \sigma Q}{c_{d4}c_{n4}^*}\right]\frac{c_{ni}^*}{P} + \left(\frac{R_s \sigma Q}{c_{d4}^* c_{n4}^*}\right)\frac{c_{di}^*}{P} \\ B_i^s &= \left(\frac{R_f Q}{c_{d4}c_{n4}}\right)\frac{(c_{ni} - c_{di})}{P}, \end{aligned} \tag{39a}$$

where

$$\begin{aligned} Q &= \sigma_{s,\text{thin}} D_{\text{thin}} \delta t/\delta x, \\ P &= \frac{R_f Q}{c_{d4}^* c_{n4}} + \frac{R_s \sigma Q}{c_{d4}c_{n4}^*} + \frac{\varepsilon_D R_f R_s \ln(R_s/R_f)}{c_{n4}c_{n4}^*}. \end{aligned} \tag{39b}$$

Similarly, for the special case of $\Delta_f = \Delta_s = 0.5$, Eqs. (26), (39) reduce to

$$\begin{aligned} g_{\bar{\alpha}}(\mathbf{x}_f, t+\delta t) &= \frac{\varepsilon_D R_f R_s \ln(R_s/R_f) + Q(R_f - \sigma R_s)}{\varepsilon_D R_f R_s \ln(R_s/R_f) + Q(R_f + \sigma R_s)}\hat{g}_{\alpha}(\mathbf{x}_f, t) \\ &\quad + \frac{2\sigma Q R_s}{\varepsilon_D R_f R_s \ln(R_s/R_f) + Q(R_f + \sigma R_s)}\hat{g}_{\bar{\alpha}}(\mathbf{x}_s, t), \end{aligned} \tag{40a}$$

$$\begin{aligned} g_{\alpha}(\mathbf{x}_s, t+\delta t) &= \frac{\varepsilon_D R_f R_s \ln(R_s/R_f) - Q(R_f - \sigma R_s)}{\varepsilon_D R_f R_s \ln(R_s/R_f) + Q(R_f + \sigma R_s)}\hat{g}_{\bar{\alpha}}(\mathbf{x}_s, t) R_s \\ &\quad + \frac{2 Q R_f}{\varepsilon_D R_f R_s \ln(R_s/R_f) + Q(R_f + \sigma R_s)}\hat{g}_{\alpha}(\mathbf{x}_f, t). \end{aligned} \tag{40b}$$

C. Conjugate heat transfer through flat, thin layer with nonuniform tangential flux

While a number of cases can be simulated using the framework shown in Secs. V A and V B, a need may arise where the tangential flux is nonuniform so that the heat fluxes in the normal direction on each side of the thin layer are not balanced (see illustration in Fig. 3 below where $q_l \neq q_r$ so that $q_d \neq q_u$). It should be emphasized that the well-posedness of the conjugate heat transfer problem typically does not allow the specification of the tangential flux in addition to the conjugate conditions in the normal direction on both sides of the thin layer. For these cases, an approximation of the tangential flux based on interpolation of the fluxes in the adjacent lattice nodes can be used. We begin with a modified setup shown in

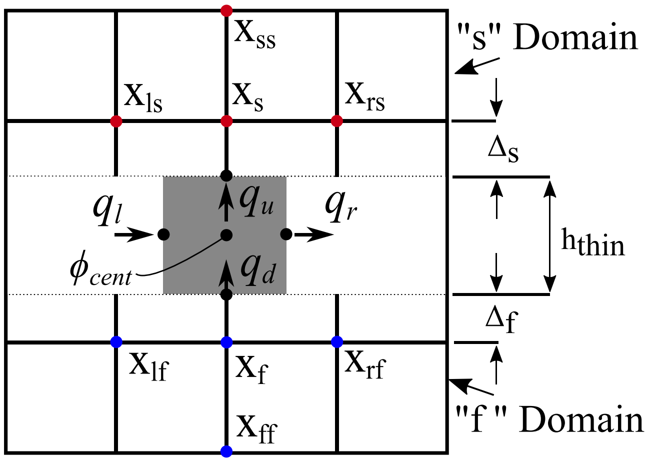

FIG. 3. Domain setup and layout of lattice nodes for conjugate heat transfer across a flat, thin plate with general nonuniform tangential flux involved.

Fig. 3, where q_i denotes the heat flux on the surfaces with l, r, u, and d representing the *left*, *right*, *upward,* and *downward* walls, respectively.

As shown in Secs. V A and V B, in order to resolve the thin layer, two relations must be present that can relate the unknown distribution functions $g_{\bar{\alpha}}(\mathbf{x}_f, t+\delta t)$ and $g_\alpha(\mathbf{x}_s, t+\delta t)$. To develop the first relation, we view the section noted in Fig. 3 from a control volume perspective, for which the energy balance at steady state gives

$$q_d\delta x + q_l h_{\text{thin}} - q_u\delta x - q_r h_{\text{thin}} = 0, \tag{41}$$

where $q = -k\frac{\partial\phi}{\partial n} = -(\rho c_p)D\frac{\partial\phi}{\partial n}$. It is noted that q_d and q_u can be related to the microscopic DFs following the Neumann-type flux relations in Eq. (16). Substitution of those into Eq. (41) gives the following relation between $g_{\bar{\alpha}}(\mathbf{x}_f, t+\delta t)$ and $g_\alpha(\mathbf{x}_s, t+\delta t)$:

$$\begin{aligned} g_{\bar{\alpha}}(\mathbf{x}_f, t+\delta t) &= (q_l - q_r)\frac{h_{\text{thin}}c_{n4}}{(\rho c_p)_f}\frac{\delta t}{(\delta x)^2} \\ &\quad - \frac{\sigma c_{n4}}{c^*_{n4}}\{g_\alpha(\mathbf{x}_s, t+\delta t) - [c^*_{n1}\hat{g}_{\bar{\alpha}}(\mathbf{x}_s, t) \\ &\quad + c^*_{n2}\hat{g}_{\bar{\alpha}}(\mathbf{x}_{ss}, t) + c^*_{n3}\hat{g}_\alpha(\mathbf{x}_s, t)]\} + [c_{n1}\hat{g}_\alpha(\mathbf{x}_f, t) \\ &\quad + c_{n2}\hat{g}_\alpha(\mathbf{x}_{ff}, t) + c_{n3}\hat{g}_{\bar{\alpha}}(\mathbf{x}_f, t)]. \end{aligned} \tag{42}$$

Additionally, it can be assumed that the heat flow rate (proportionally to flux in planar domain) distribution is continuous across the thin layer, and thus q_l and q_r can be approximated from the interpolation of the fluxes at the nearby lattice nodes. Taking q_l as an example in Fig. 4, a local area-based interpolation of the heat fluxes at those nodes gives

$$\begin{aligned} q_l &= -k_{\text{thin}}\frac{\partial\phi}{\partial x}\bigg|_{\frac{x_{lf}+x_f}{2}} \\ &= -\frac{k_{\text{thin}}}{A_{ls}+A_{lf}+A_s+A_f}\left(A_{ls}\frac{\partial\phi}{\partial x}\bigg|_{x_f} + A_{lf}\frac{\partial\phi}{\partial x}\bigg|_{x_s}\right. \\ &\quad \left. + A_s\frac{\partial\phi}{\partial x}\bigg|_{x_{lf}} + A_f\frac{\partial\phi}{\partial x}\bigg|_{x_{ls}}\right). \end{aligned} \tag{43a}$$

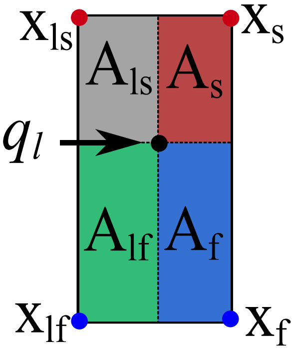

FIG. 4. Illustration of the area-based interpolation for q_1.

Similar interpolation can be applied to obtain q_r:

$$\begin{aligned} q_r &= -k_{\text{thin}}\frac{\partial\phi}{\partial x}\bigg|_{\frac{x_f+x_{rf}}{2}} \\ &= -\frac{k_{\text{thin}}}{A_{rs}+A_{rf}+A_s+A_f}\left(A_{rs}\frac{\partial\phi}{\partial x}\bigg|_{x_f} + A_{rf}\frac{\partial\phi}{\partial x}\bigg|_{x_s}\right. \\ &\quad \left. + A_s\frac{\partial\phi}{\partial x}\bigg|_{x_{rf}} + A_f\frac{\partial\phi}{\partial x}\bigg|_{x_{rs}}\right). \end{aligned} \tag{43b}$$

Furthermore, it is noted that all the lattice nodes $\mathbf{x}_{lf}$, $\mathbf{x}_{ls}$, $\mathbf{x}_f$, and $\mathbf{x}_s$ are interior nodes within the two domains. The scalar gradients $\partial\phi/\partial x$ at the interior nodes can be conveniently obtained from the microscopic DFs as verified in Refs. [15,42,43]. In this work, we use the formula proposed in Ref. [42] to obtain those in Eq. (43):

$$-D_{f,s}\frac{\partial\phi}{\partial x_i} = \left(1 - \frac{1}{2\tau_{f,s}}\right)\frac{\delta x}{\delta t}\sum_{\alpha=1}^{m-1}\mathbf{e}_{\alpha i}\left(g_\alpha - g_\alpha^{\text{eq}}\right). \tag{44}$$

Hence, the combination of Eqs. (42)–(44) would give the first relationship between the two unknowns $g_{\bar{\alpha}}(\mathbf{x}_f, t+\delta t)$ and $g_\alpha(\mathbf{x}_s, t+\delta t)$. To construct the second relationship, the scalar values at the interfaces of the thin layer, $\phi_{f,\text{thin}}$ and $\phi_{s,\text{thin}}$, should be included. However, it should be noted that with varying tangential flux involved, the simple relation in Eq. (30) can no longer be used. To deal with this, we approximate the flux components q_d and q_u as

$$q_d = -k_{\text{thin}}\frac{\partial\phi}{\partial y}\bigg|_{f,\text{thin}} = -2k_{\text{thin}}\frac{\phi_{cent} - \phi_{f,\text{thin}}}{h_{\text{thin}}} \tag{45a}$$

and

$$q_u = -k_{\text{thin}}\frac{\partial\phi}{\partial y}\bigg|_{s,\text{thin}} = -2k_{\text{thin}}\frac{\phi_{s,\text{thin}} - \phi_{cent}}{h_{\text{thin}}}, \tag{45b}$$

where ϕ_{cent} is the introduced scalar value at the center of the thin layer (see Fig. 3).

Combining Eqs. (45a) and (45b), one obtains the relation

$$q_u + q_d = \frac{-2k_{\text{thin}}}{h_{\text{thin}}}(\phi_{s,\text{thin}} - \phi_{f,\text{thin}}). \tag{46}$$

Since q_d, q_u, $\phi_{f,\text{thin}}$, and $\phi_{s,\text{thin}}$ can all be obtained from the microscopic DFs in the LBM, we can rewrite Eq. (46) as

$$\begin{aligned}
&\frac{g_\alpha(\mathbf{x}_s, t+\delta t) - c_{n1}^*\hat{g}_{\bar{\alpha}}(\mathbf{x}_s, t) - c_{n2}^*\hat{g}_{\bar{\alpha}}(\mathbf{x}_{ss}, t) - c_{n3}^*\hat{g}_\alpha(\mathbf{x}_s, t)}{c_{n4}^*}(\rho c_p)_s \\
&\quad - \frac{g_{\bar{\alpha}}(\mathbf{x}_f, t+\delta t) - c_{n1}\hat{g}_\alpha(\mathbf{x}_f, t) - c_{n2}\hat{g}_\alpha(\mathbf{x}_{ff}, t) - c_{n3}\hat{g}_{\bar{\alpha}}(\mathbf{x}_f, t)}{c_{n4}}(\rho c_p)_f \\
&= \frac{-2k_{\text{thin}}}{h_{\text{thin}}}\frac{\delta t}{\delta x}\left[\frac{g_\alpha(\mathbf{x}_s, t+\delta t) - c_{d1}^*\hat{g}_{\bar{\alpha}}(\mathbf{x}_s, t) - c_{d2}^*\hat{g}_{\bar{\alpha}}(\mathbf{x}_{ss}, t) - c_{d3}^*\hat{g}_\alpha(\mathbf{x}_s, t)}{\varepsilon_D c_{d4}^*}\right. \\
&\quad \left. - \frac{g_{\bar{\alpha}}(\mathbf{x}_f, t+\delta t) - c_{d1}\hat{g}_\alpha(\mathbf{x}_f, t) - c_{d2}\hat{g}_\alpha(\mathbf{x}_{ff}, t) - c_{d3}\hat{g}_{\bar{\alpha}}(\mathbf{x}_f, t)}{\varepsilon_D c_{d4}}\right].
\end{aligned} \tag{47}$$

Combining Eqs. (42) and (47), the general interface scheme for conjugate heat transfer through a thin wall can be written as

$$\begin{aligned}
g_{\bar{\alpha}}(\mathbf{x}_f, t+\delta t) &= A_1^f\hat{g}_\alpha(\mathbf{x}_f, t) + A_2^f\hat{g}_\alpha(\mathbf{x}_{ff}, t) + A_3^f\hat{g}_{\bar{\alpha}}(\mathbf{x}_f, t) \\
&\quad + B_1^f\hat{g}_{\bar{\alpha}}(\mathbf{x}_s, t) + B_2^f\hat{g}_{\bar{\alpha}}(\mathbf{x}_{ss}, t) + B_3^f\hat{g}_\alpha(\mathbf{x}_s, t) \\
&\quad + \frac{(q_l - q_r)}{(\rho c_p)_f}\frac{\delta t}{(\delta x)^2}\left(\frac{\varepsilon_D h_{\text{thin}}}{c_{n4}^*} + \frac{2Q}{c_{d4}^*}\right)\frac{h_{\text{thin}}}{2P},
\end{aligned} \tag{48a}$$

$$\begin{aligned}
g_\alpha(\mathbf{x}_s, t+\delta t) &= A_1^s\hat{g}_{\bar{\alpha}}(\mathbf{x}_s, t) + A_2^s\hat{g}_{\bar{\alpha}}(\mathbf{x}_{ss}, t) + A_3^s\hat{g}_\alpha(\mathbf{x}_s, t) \\
&\quad + B_1^s\hat{g}_\alpha(\mathbf{x}_f, t) + B_2^s\hat{g}_\alpha(\mathbf{x}_{ff}, t) + B_3^s\hat{g}_{\bar{\alpha}}(\mathbf{x}_f, t) \\
&\quad + \frac{(q_l - q_r)}{(\rho c_p)_f}\frac{\delta t}{(\delta x)^2}\left(\frac{\varepsilon_D h_{\text{thin}}}{c_{n4}} + \frac{2\sigma Q}{c_{d4}}\right)\frac{h_{\text{thin}}}{2\sigma P},
\end{aligned} \tag{48b}$$

with the same coefficients as presented in Eqs. (32a), (32b) for A_i^f, B_i^f, A_i^s, and B_i^s, $i = 1–3$.

Similar to the previous sections, a simplified scheme is ascertained if $\Delta_f = \Delta_s = 0.5$, such that Eqs. (48a), (48b) reduce to

$$\begin{aligned}
g_{\bar{\alpha}}(\mathbf{x}_f, t+\delta t) &= \frac{\varepsilon_D h_{\text{thin}} + (1-\sigma)Q}{\varepsilon_D h_{\text{thin}} + (1+\sigma)Q}\hat{g}_\alpha(\mathbf{x}_f, t) \\
&\quad + \frac{2\sigma Q}{\varepsilon_D h_{\text{thin}} + (1+\sigma)Q}\hat{g}_{\bar{\alpha}}(\mathbf{x}_s, t) \\
&\quad + \frac{(q_l - q_r)}{(\rho c_p)_f}\frac{\delta t}{(\delta x)^2}\frac{h_{\text{thin}}}{2}\frac{\varepsilon_D h_{\text{thin}} + 2Q}{\varepsilon_D h_{\text{thin}} + (1+\sigma)Q},
\end{aligned} \tag{49a}$$

$$\begin{aligned}
g_\alpha(\mathbf{x}_s, t+\delta t) &= \frac{\varepsilon_D h_{\text{thin}} - (1-\sigma)Q}{\varepsilon_D h_{\text{thin}} + (1+\sigma)Q}\hat{g}_{\bar{\alpha}}(\mathbf{x}_s, t) \\
&\quad + \frac{2Q}{\varepsilon_D h_{\text{thin}} + (1+\sigma)Q}\hat{g}_\alpha(\mathbf{x}_f, t) \\
&\quad + \frac{(q_l - q_r)}{(\rho c_p)_f}\frac{\delta t}{(\delta x)^2}\frac{h_{\text{thin}}}{2\sigma}\frac{\varepsilon_D h_{\text{thin}} + 2\sigma Q}{\varepsilon_D h_{\text{thin}} + (1+\sigma)Q}.
\end{aligned} \tag{49b}$$

VI. NUMERICAL VERIFICATION AND DISCUSSION

In order to demonstrate the numerical validity and accuracy of the thin-wall schemes, three test cases with analytical solutions available are examined: Sec. VI A: 1D diffusion in a three-layered slab, Sec. VI B: 2D axisymmetric diffusion with a sandwiched thin region, and Sec. VI C: 2D convection diffusion within a channel where two different fluids are separated by a thin layer. The first test studies the scheme presented in Sec. V A, where the tangential flux within the thin area is zero. Test VI B studies the same concept with applications in circular domains with the axisymmetric LBM model, thus studying the applicability of the proposed scheme in Sec. V B. The final test analyzes the accuracy and convergence behavior of the general scheme in Sec. V C with nonuniform tangential fluxes. Moreover, since the scheme in Sec. V A can be considered an approximation of the general scheme in Sec. V C when neglecting the tangential flux variations, a direct comparison of those two schemes is also conducted with both implemented in the last test. The advantage and improvement of the general scheme over its simplified version is verified from an accuracy standpoint.

A. 1D diffusion in a three-layered slab

The planar configuration and the lattice domain is illustrated in Fig. 5, where H_1, H_2, and H_3 are the respective

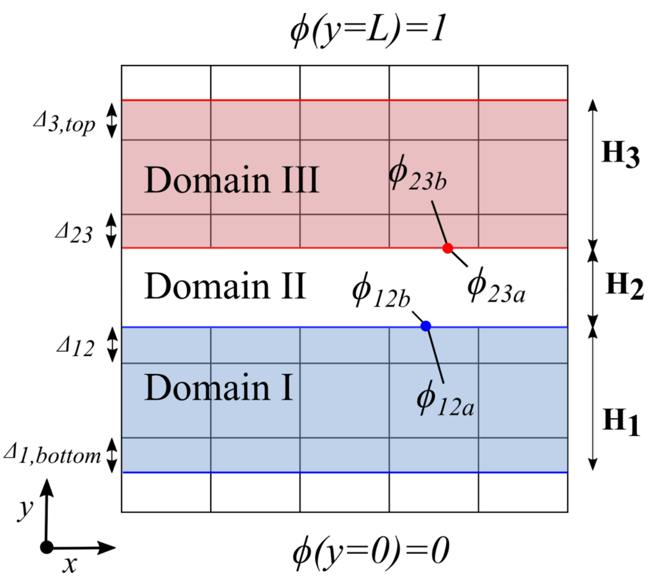

FIG. 5. Schematic depiction of the computational domain and the lattice distribution for 1D diffusion in a three-layered slab.

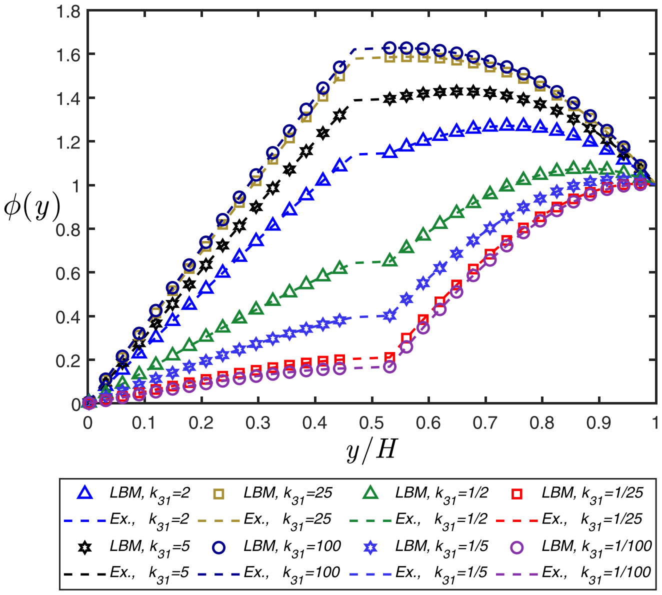

FIG. 6. Dimensionless temperature profiles within the three-layered slab for conjugate heat transfer across the thin middle layer with varied thermal conductivity ratios.

domain heights with distinct materials of thermal conductivities k_1, k_2, and k_3.

The boundary and interfacial link fraction offsets $\Delta_{3,\mathrm{top}}$, $\Delta_{1,\mathrm{bottom}}$, Δ_{12}, and Δ_{23} represent the local distances of the boundary and interface nodes to the closest LBM nodes as shown. For LBM computation, Dirichlet conditions are applied on both the top and bottom walls following $\phi_1(y=0)=0$ and $\phi_3(y=H=H_1+H_2+H_3)=1$; periodic boundary conditions are imposed on the left and right walls; and the proposed interface scheme in Eqs. (26a), (26b) with coefficients determined in Eqs. (32a), (32b) for flat, thin layers resolves the dual set of conjugate conditions. To obtain nontrivial results, a quadratic heat source is also imposed. The analytical solution is provided in the Appendix.

For illustration, Fig. 6 presents profiles of $\phi_{1,2,3}(y)$ for eight sets of thermal conductivity ratios, $k_{31}=k_3/k_1$, for the materials in the first and third domains with $\Delta_{3,\mathrm{top}}=\Delta_{1,\mathrm{bottom}}=\Delta_{12}=\Delta_{23}=0.5$. For the simulation, the domain heights are fixed as $H_1=H_3=128\delta x$ and $H_2=16\delta x$. The remaining parameters used are $k_{21}=k_2/k_1=250$ for $k_{31}>1$, $k_{23}=k_2/k_3=250$ for $k_{31}<1$, $\tau_1=\tau_3=0.65$, and $\sigma=k_{31}$. For clarification, Q is determined for all simulations presented from the relation $\sigma_{s,\mathrm{thin}}D_{\mathrm{thin}}\frac{\delta t}{\delta x}=\frac{(\rho c_p)_{\mathrm{thin}}D_{\mathrm{thin}}\delta t/\delta x}{(\rho c_p)_s}=\frac{k_{\mathrm{thin}}\delta t/\delta x}{(\rho c_p)_s}$, where $k_{\mathrm{thin}}=k_2$. The reader should note that with the proposed interface scheme in this work, no lattice nodes or LBM computation are needed for the thin layer. For the quadratic source $S(y)=[\frac{12a}{L^2}(\frac{y}{L})^2+\frac{6b}{L^2}(\frac{y}{L})+\frac{2c}{L^2}]$ in domains I and III, $a=1$, $b=0$, and $c=0$ were used. It is discerned that the LBM results agree very well with the exact solutions.

For further inspection, Fig. 7 shows the profiles of $\phi_{1,2,3}(y)$ with varied thin-layer thicknesses H_2. This simulation maintains the same resolution in domains I and III as $H_1=H_3=128\delta x$, and domain II is varied as $H_2=(1,2,8,32,64,128,256,1024)\delta x$. The other simulation parameters are set as $k_{31}=1$, $k_{21}=5$, $\tau_1=\tau_3=0.65$, $\sigma=1$, $a=1$, $b=0$, and $c=0$. A key point to be made here is that the interface scheme across the thin layer proposed in this work is derived from integration of the temperature gradient over the thin-layer domain [see Eq. (30)], which is an exact relation when no varying tangential heat flux is present ($q_r=q_l$). This is the reason that the LBM results shown in Fig. 7 retain a high degree of accuracy even at large H$_2$ values without associated meshing in the domain. The large H_2 values shown in Fig. 7 are presented to demonstrate this point; however, care should be taken as the formulation would not be well-posed for cases with thick walls and non-negligible amounts of tangential heat flux variation. A similar statement can be made for an unsteady formulation with thick walls.

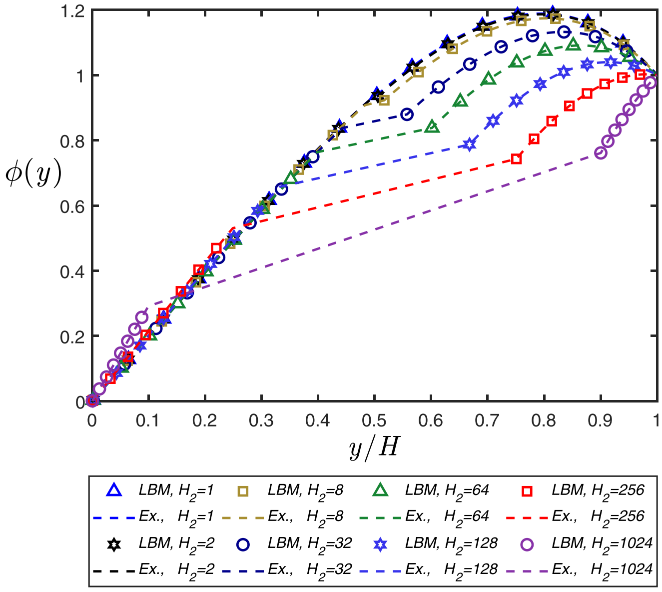

FIG. 7. Dimensionless temperature profiles, $\phi_{1,2,3}$, at varied thin-region thicknesses.

To further assess the accuracy of the proposed interface scheme, we define the relative L_2-norm error as

$$E_2=\left[\frac{\sum_{x,y}(\phi_{\mathrm{LBM}}-\phi_{\mathrm{ex}})^2}{\sum_{x,y}\phi_{\mathrm{ex}}^2}\right]^{1/2}, \tag{50}$$

where E_2 contains the relative errors of the thermal field where LBM nodes are present. The Dirichlet boundary conditions applied at the bottom and top of the domain have been studied extensively [19,22]; therefore, they are not studied again here. For convenience, we let $\Delta_{1,\mathrm{bottom}}=1–\Delta_{12}$ and $\Delta_{3,\mathrm{top}}=1–\Delta_{23}$ to keep H_1 and H_3 as integers. The effects of different interfacial offsets, Δ, are investigated with the E_2 error distribution. However, it should be noted that these are strictly chosen for numerical verification and no limit is imposed on the scheme related to interfacial offsets. Several wall thicknesses are studied, ranging from $H_1/H_2=H_3/H_2=5, 25, 50,$ and 100 and for interfacial offsets ranging between $\Delta=0.01,\ 0.25,\ 0.50,\ 0.75,$ and 0.99. Figure 8 presents the results of the study for simulation parameters $k_{21}=8$, $k_{31}=0.02$, $\tau_1=0.75$, $\tau_3=0.875$, $\sigma=0.013\bar{3}$, $a=1$, $b=0$, and $c=0$.

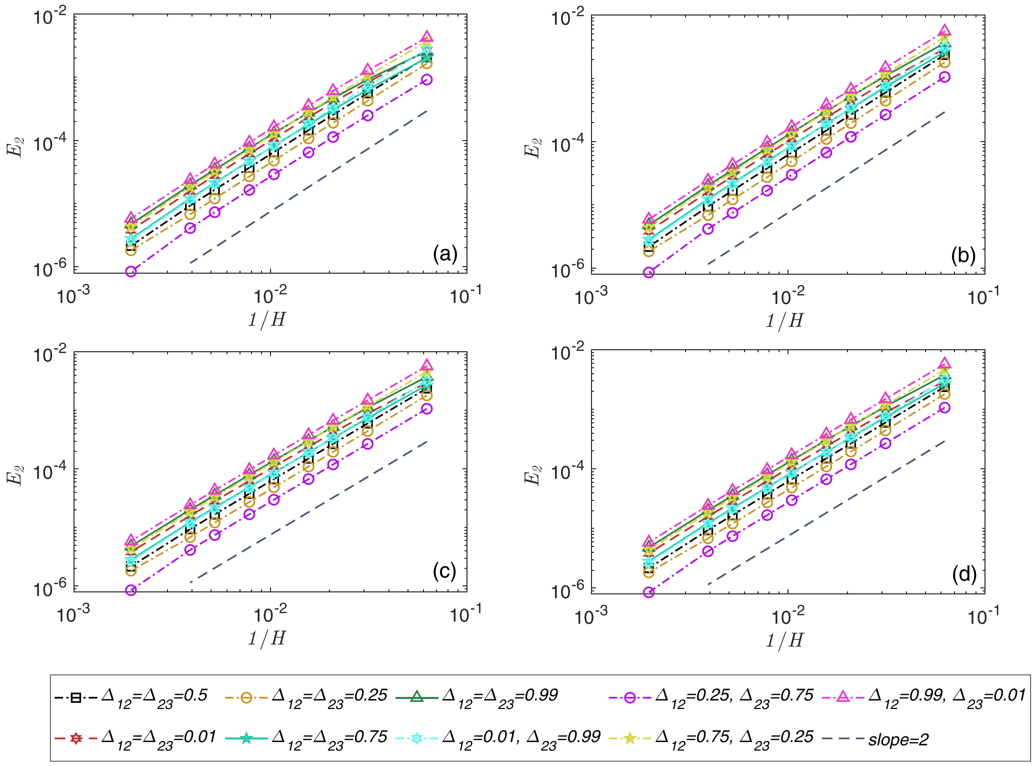

FIG. 8. Relative L_2-norm errors for varying wall thicknesses. (a) $H_1/H_2 = H_3/H_2 = 5$, (b) $H_1/H_2 = H_3/H_2 = 25$, (c) $H_1/H_2 = H_3/H_2 = 50$, and (d) $H_1/H_2 = H_3/H_2 = 100$, vs the grid resolution, $1/H$, at different lattice link fraction Δ_{12} and Δ_{23} values.

It is consistently observed that all the interfacial offsets and wall thicknesses studied demonstrate second-order accuracy. Some variation in the overall error is evident between different cases; however, the magnitudes can be considered relatively small, ranging between 10^{-5} and 10^{-6} when $H_1 + H_3 = 512\delta x$. The authors also note that various k_1, k_2, k_3, σ, τ_1, and τ_3 parameters were applied and second-order accuracy was obtained for all cases; however, we omit the additional results for brevity.

B. 2D axisymmetric diffusion with a sandwiched circular layer

To validate the proposed interface scheme in Sec. V B for annular thin layers with the axisymmetric LBM, a three-region annulus test case is proposed as displayed in Fig. 9, where R refers to the radii of the setup with corresponding subscripts i, 1, 2, and o differentiating the radii. It is pointed out that the LBM model implemented is one-dimensional since no variation is observed in the θ direction. Similar to the previous section, Dirichlet boundary conditions are applied at both the inner and outer annulus surfaces as $\phi(r = R_i) = \phi_i$ and $\phi(r = R_o) = \phi_o$; periodic boundary conditions are applied in the length direction (into the page) maintaining an infinitely long cylinder; and the interface scheme described in Sect. V B is used to account for the conjugate conditions and heat transfer across the thin layer.

For steady axisymmetric diffusion with conjugate conditions at the interfaces, the exact solution can be solved as

$$\phi_{i1}(r) = \frac{C_1}{k_1}\ln(r) + C_2,\ \ R_i \leqslant r < R_1, \tag{51a}$$

$$\phi_{12}(r) = \frac{C_1}{k_2}\ln(r) + C_3,\ \ R_1 \leqslant r < R_2, \tag{51b}$$

$$\phi_{2o}(r) = \frac{C_1}{k_3}\ln(r) + \phi_o,\ \ R_2 \leqslant r < R_o, \tag{51c}$$

where

$$C_1 = \frac{\phi_o}{\frac{\ln(R_1/R_i)}{k_1} - \frac{\ln(R_1/R_2)}{k_2} - \frac{\ln(R_2)}{k_3}}, \tag{52a}$$

$$C_2 = \phi_i - \frac{C_1}{k_1}\ln(R_1), \tag{52b}$$

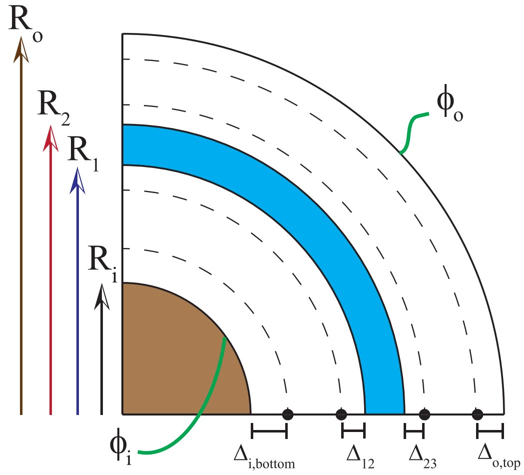

FIG. 9. Schematic depiction of the circular domain with axisymmetric diffusion in a three-layered bounded annulus.

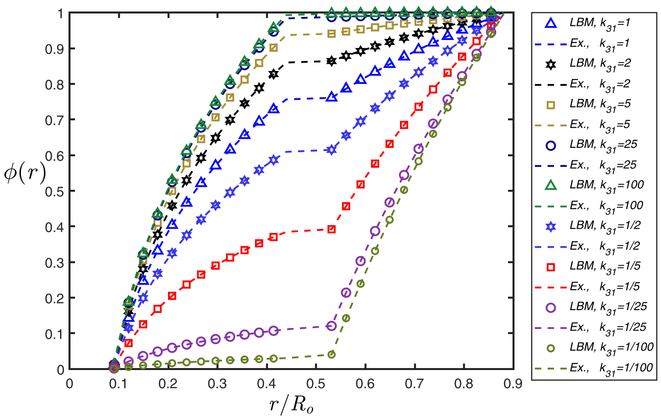

FIG. 10. Dimensionless temperature profiles, $\phi_{1,2,3}$, as a function of domain height, r/R_o, for varied thermal conductivity ratios.

$$C_3 = C_1\left[\frac{\ln(R_1/R_i)}{k_1} - \frac{\ln(R_1)}{k_2}\right] - \phi_i. \tag{52c}$$

Dirichlet boundary conditions of $\phi_i = 0$ and $\phi_o = 1$ are applied for all studies presented in this section, and the proposed conjugate interface scheme in Sec. V B is implemented. First, a visual illustration of the temperature distribution is shown in Fig. 10 for fixed radii of $R_i = 24$, $R_1 = 120$, $R_2 = 144$, and $R_o = 240$ all in LB unit. The relaxation-time coefficients τ_1 and τ_3 in the LBM for domains I and III are fixed as $\tau_1 = 0.65$ and $\tau_3 = 1.0$, the thermal conductivity of domain II is fixed as $k_{21} = k_2/k_1 = 100$ for $k_{31} \geqslant 1$ and $k_{23} = k_2/k_3 = 100$ for $k_{31} \leqslant 1$, and the heat capacity ratio is varied as $\sigma = 0.3k_{31}$. To analyze the scheme sensitivity and robustness, a wide range of k_{31} ratios are tested as shown. As expected, excellent agreement between the simulated and theoretical temperature profiles is observed.

To evaluate the order of accuracy of the proposed interface scheme, the L_2-norm errors are ascertained by varying multiple setup parameters. First, we study the effect of the link fractions on the accuracy of the proposed scheme. As in Sec. VI A, we maintain the relationship that the domain itself is an integer by constraining the physical offsets at R_i and R_o as $\Delta_{1,\text{bottom}} = 1–\Delta_{12}$ and $\Delta_{3,\text{top}} = 1–\Delta_{23}$. These constraints are strictly for ease of results formatting and there is no inherent limit that the radial differences must be integers. Figure 11 shows the results of E_2 versus the grid resolution $1/R_{\text{LB,nodes}} \equiv 1/[(R_1 - R_i) + (R_o - R_2)]$ for link fractions $\Delta = 0.01$, 0.25, 0.50, 0.75, and 0.99 with differing thicknesses of the thin region as $(R_o - R_i)/(R_2 - R_1) = 9$ and $(R_o - R_i)/(R_2 - R_1) = 3$. The relaxation-time coefficients and material ratios are fixed as $\tau_1 = 0.75$, $\tau_3 = 1.25$, $k_{21} = 8$, $k_{31} = 0.04$, and $\sigma = 0.01\bar{3}3$. Clearly, second-order accuracy is preserved for all cases tested. The retainment of this inherent second-order accuracy is observed since the model exactly resolves the heat transfer within the thin layer [see Eq. (36)] when the heat flow rate is constant at steady state in the radial direction for the problem.

To further gain an understanding of the effect of wall thickness and to compare the present "nonmeshing" scheme to the original interface scheme in LBM, we compare the L_2-norm errors obtained using both the interface scheme presented in this work and an LBM model including lattice nodes within the sandwiched thin layer with two sets of conjugate conditions resolved by the zero-thickness interface scheme [see Eqs. (26), (27)]. For simplicity, we choose the inner-outer radius ratio as $R_o/R_i = (R_o - R_i)/(R_2 - R_1) + 1$ for all simulations and the interfacial offsets are all set to 0.5 so that the lengths of the regions containing lattice nodes are all integers. The ratio of the thin-layer thickness to overall domain extent are varied as $(R_o - R_i)/(R_2 - R_1) = 3$, 6, 9, 12, and 15. The relaxation-time coefficients and heat capacity ratios are $\tau_1 = 0.625$ and $\tau_3 = 0.85$, and $\sigma = (5/14)k_{31}$, respectively. Figure 12 presents the results of the study, with Figs. 12(a) and 12(c) constraining the thermal conductivities as $k_{21} = 100$, $k_{31} = 25$ and Figs. 12(b) and 12(d) as $k_{21} = 4$, $k_{31} = 0.04$. Figures 12(a) and 12(b) correspond to the results obtained with the framework developed in Sec. V B, while Figs. 12(c) and 12(d) are from the zero-thickness interface setup as described, which requires lattice nodes within the middle layer and two sets of conjugate conditions. It is evident that both methods demonstrate second-order accuracy. From a magnitude of error standpoint, both schemes demonstrate considerably low errors and their magnitudes are very close to each other. Furthermore, it can be observed that the results in Figs. 12(c) and 12(d) are less sensitive to the geometry change

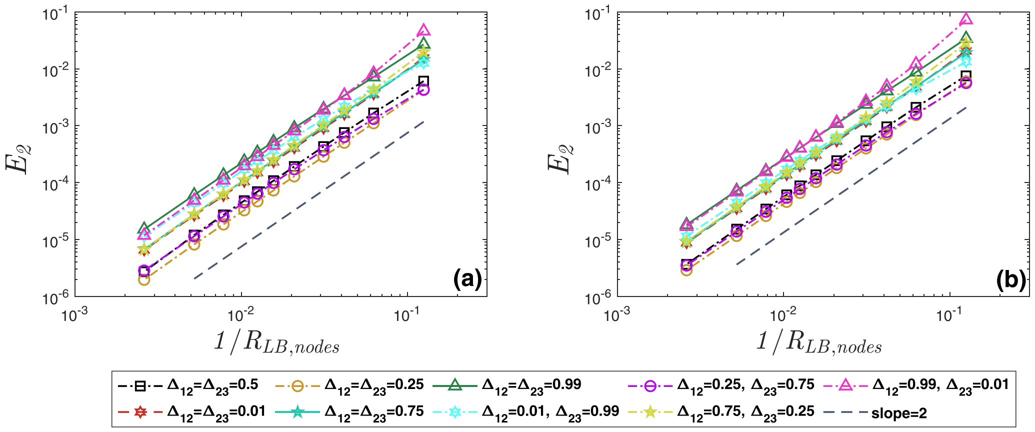

FIG. 11. L_2-norm errors for varying thin annulus thicknesses, (a) $(R_o - R_i)/(R_2 - R_1) = 9$ and (b) $(R_o - R_i)/(R_2 - R_1) = 3$, vs the grid resolution, $1/R_{\text{LB,nodes}} \equiv 1/[(R_1 - R_i) + (R_o - R_2)]$.

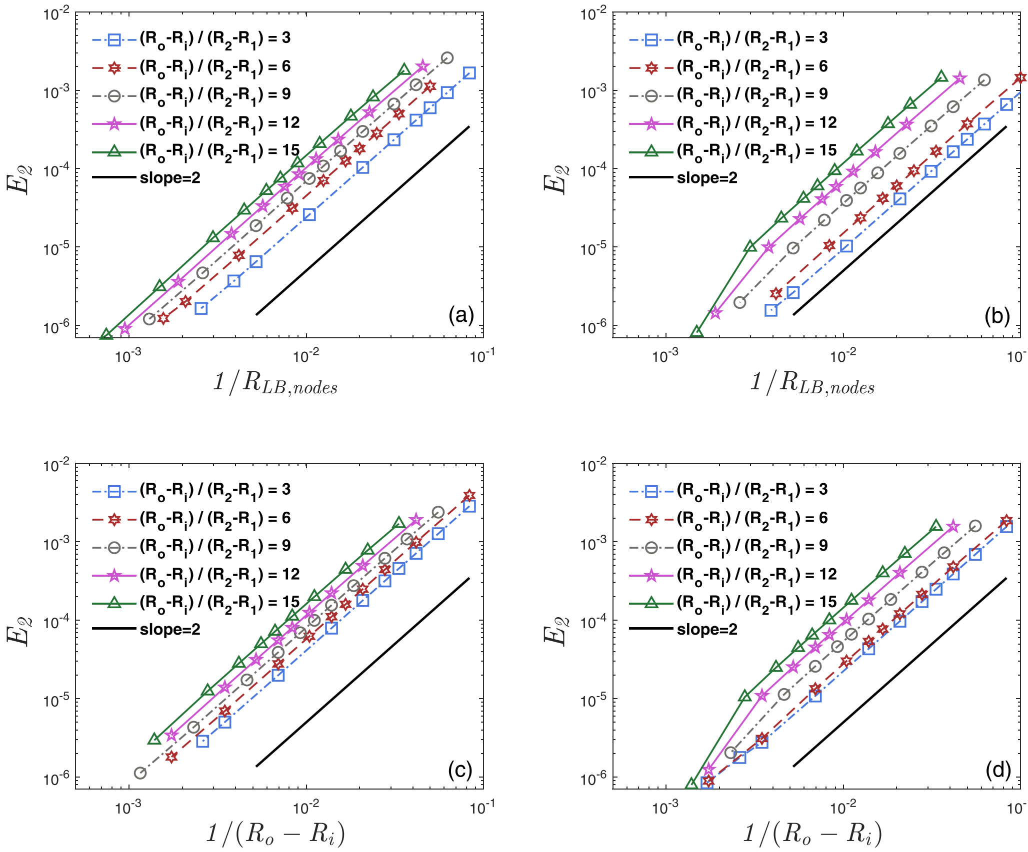

FIG. 12. L_2-norm errors for varying thermal conductivity ratios, (a) $k_{21} = 100$, $k_{31} = 25$ and (b) $k_{21} = 4$, $k_{31} = 0.04$, vs the grid resolution, $1/R_{\text{LB,nodes}} \equiv 1/[(R_1 - R_i) + (R_o - R_2)]$, for the finite-thickness scheme; (c) $k_{21} = 100$, $k_{31} = 25$, and (d) $k_{21} = 4$, $k_{31} = 0.04$, vs the grid resolution, $1/(R_o–R_i)$, for the zero-thickness scheme.

[different $(R_o - R_i)/(R_2 - R_1)$ ratios] when using the original zero-thickness scheme compared to those in Figs. 12(a) and 12(b) with the present scheme, i.e., the curves are packed within a thinner band. This study confirms the applicability and accuracy of the proposed interface scheme, which can significantly simplify the interface treatment and save computational resources.

In addition to the interior temperature field, various design applications require that interfacial temperatures and heat fluxes for solid components, such as metal-oxide-semiconductor field-effect transistors and stator coil windings, be effectively predicted to verify that they are within their required thermal operating ranges. Using Eqs. (24) and (25), the macroscopic temperature and flux can be "back-calculated" using the known postcollision DFs and the solved DFs $g_{\bar{\alpha}}(\mathbf{x}_f, t + \delta t)$ and $g_\alpha(\mathbf{x}_s, t + \delta t)$ at the new time step from the interface scheme in Sec. V. To gain an understanding of the order of accuracy of these interfacial quantities, two additional sets of L_2-norm errors are defined as

$$E_{2\_tint} = \left[\frac{\sum_{\text{interface}} (\phi_{\text{int}_{\text{LBM}}} - \phi_{\text{int}_{\text{ex}}})^2}{\sum_{\text{interface}} \phi^2_{\text{int}_{\text{ex}}}}\right]^{1/2}, \tag{53}$$

$$E_{2\_qint} = \left[\frac{\sum_{\text{interface}} \left(k_i \frac{\partial\phi_i}{\partial n_i}\big|_{\text{LBM}} - k_i \frac{\partial\phi_i}{\partial n_i}\big|_{\text{ex}}\right)^2}{\sum_{\text{interface}} \left(k_i \frac{\partial\phi_i}{\partial n_i}\big|_{\text{ex}}\right)^2}\right]^{1/2}, \quad (i = 1, 2), \tag{54}$$

which can be used to evaluate the L_2-norm errors on each of the two interfaces of the thin layer. Using identical parameters to those of Fig. 12(a), the errors are plotted for the interfacial temperature and flux in Figs. 13 and 14, respectively. Figures 13(a) and 14(a) represent the scalar and flux quantities at $r = R_1$ calculated with the updated streaming function $g_{\bar{\alpha}}(\mathbf{x}_f, t + \delta t)$ and similarly so in Figs. 13(b) and 14(b) for the quantities at $r = R_2$ with $g_\alpha(\mathbf{x}_s, t + \delta t)$. It is observed that second- and third-order convergence rates with low error magnitude are obtained for E_{2_tint} and E_{2_qint}, respectively, for the case of zero-tangential flux studied here. The third-order convergence is due to the selection of $\Delta = 0.5$ everywhere and the other simulation parameters. Additional tests were also conducted with arbitrary Δ values and in general only second-order accuracy is preserved; for brevity, the results are not shown here. Overall, this test further strengthens the propensity of the scheme for wide use, as it is still strongly applicable in situations where the interface temperature and heat flux need to be determined at the thin layer.

C. 2D convection diffusion within a channel with plug-flow fluids

To evaluate the applicability and accuracy of the general interface scheme in Sec. V C for cases with nonuniform tangential flux, a 2D dual-section convection-diffusion problem with a plug flow is simulated based on previous works [19,22].

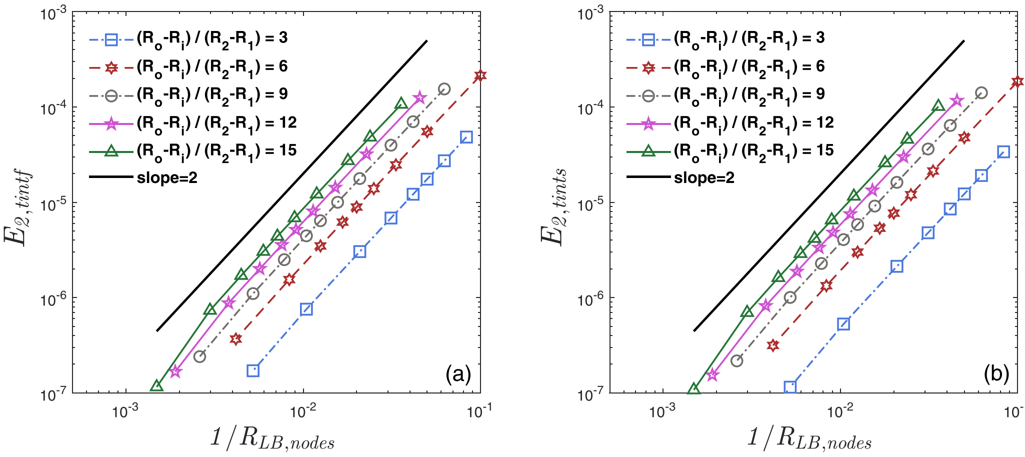

FIG. 13. L_2-norm errors for the interfacial scalar values (a) ϕ_{intf} at $r = R_1$ and (b) ϕ_{ints} at $r = R_2$ vs the grid resolution $1/R_{\text{LB,nodes}} \equiv 1/[(R_1 - R_i) + (R_o - R_2)]$ with simulation parameters $k_{21} = 4$, $k_{31} = 0.04$, $\tau_1 = 0.625$, $\tau_3 = 0.85$, and $\sigma = (5/14)\, k_{31}$.

The test case presented in Refs. [19,22] is extended to include an additional domain (three total domains) with the allowance of varied heights as schematically depicted in Fig. 15. Sinusoidal Dirichlet boundary conditions are applied to both the top and bottom walls as $\phi_1(x, y = 0) = \phi_3(x, y = H) = \cos(kx)$, with $k = 2\pi/L$, and periodic boundary conditions are applied at the left and right sides of the domains.

Assuming a constant plug flow $\mathbf{u} = (U, 0)$ in domains I and III and $\mathbf{u} = (0, 0)$ in domain II, the characteristic Péclet number is defined as $Pe = UH/D_1$ with $H = H_1 + H_2 + H_3$. The exact solution for the scalar field is given in the Appendix.

For illustration, Fig. 16 shows the LBM solution for the dimensionless temperature field at $Pe = 10$ for a domain of $H_1 = H_3 = 128\delta x$ and $H_2 = \delta x$ with all boundary and interface link fractions $\Delta = 0.5$. The parameters used also include $k_{21} = 10$, $k_{31} = 1$, $\sigma = 1$, and $\tau_1 = \tau_3 = 0.55$. It is observed that the LBM solution overlays directly on the exact solution with no noticeable variations. It is also noted that this test case does include variation in the heat flow rate in the x direction within the thin layer, therefore making it a suitable benchmark example to examine the general interface scheme developed in Sec. V C.

A comprehensive study of the numerical stability is out of the scope of this work, while similar stability behavior presented in Ref. [22] for the zero-thickness conjugate scheme can be expected for the present schemes. The numerical stability can usually be improved by choosing approximate relaxation-time coefficients as demonstrated in Ref. [22]. For conjugate heat transfer between phases or materials with very large transport property ratios, the decoupled interface scheme presented in Ref. [44] can be implemented and the present interface scheme can be easily extended to incorporate that. In addition, the area-based interpolation for the approximation of the tangential fluxes (q_r and q_l in Fig. 3) could also lead to instability when the relative dimension of the thin layer to the neighboring domains is large enough.

The order of accuracy of the LBM solution for the interior temperature fields in domains I and III is examined first. Figure 17 shows the L_2-norm errors defined in Eq. (51) for varying H_2 with $Pe = 20$, $k_{31} = 2/3$, $k_{21} = 10$, $\sigma = 2/3$, and $\tau_1 = 0.60$, $\tau_3 = 0.60$. It should be emphasized that three different interface schemes were implemented: in Fig. 17(a), the tangential flux variation is neglected and the scheme in Sec. V A was used, while in Fig. 17(b), the general scheme

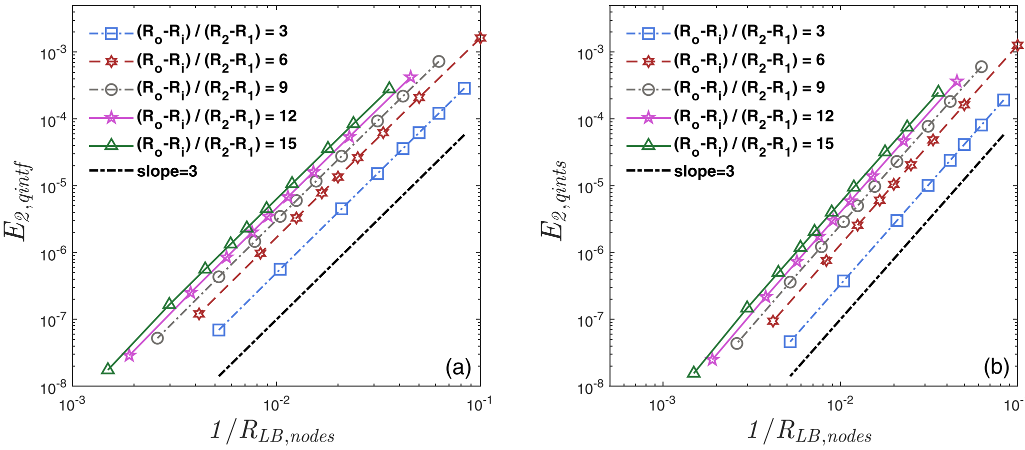

FIG. 14. L_2-norm errors for the interfacial flux values (a) q_{intf} at $r = R_1$ and (b) q_{ints} at $r = R_2$ vs the grid resolution $1/R_{\text{LB,nodes}} \equiv 1/[(R_1 - R_i) + (R_o - R_2)]$ with the same parameters in Fig. 13.

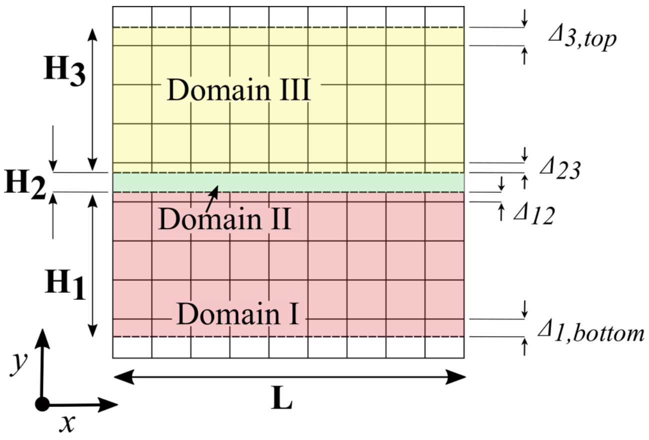

FIG. 15. Schematic depiction of the computational domain and the lattice distribution for convection-diffusion in a three-layered channel with two fluid domains.

in Sec. V C with interpolation-based approximation of the tangential fluxes, q_l and q_r, in each LB unit cell was applied [see Eqs. (40a), (40b)]; moreover, in Fig. 17(c), the general scheme in Sec. V C was also implemented but with exact tangential fluxes of q_l and q_r rather than their approximations. In general, the exact tangential flux is not available, but this can serve as a valuable reference case to compare with the simulated cases. Several key points can be observed from Fig. 17: (1) the error magnitude is significantly reduced in Fig. 17(b) compared to Fig. 17(a); (2) the errors are less sensitive to the variation of the thin-layer thickness H_2 in Fig. 17(b) compared to Fig. 17(a), both confirming the necessity of including the tangential flux variation in the interface scheme; (3) compared to the idealized situation in Fig. 17(c) with second-order convergence, only first-order accuracy is obtained for both schemes proposed in Sec. V A and Sec. V C, implying that the approximation of the tangential fluxes is responsible for the reduction in the order of accuracy. Therefore, it can be concluded that the present interface scheme is first-order accurate for general cases.

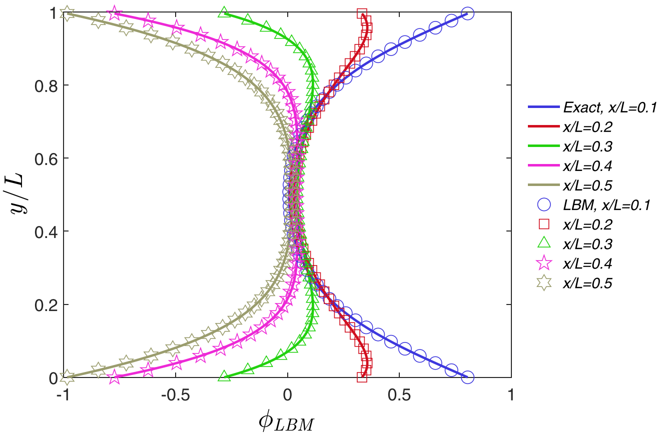

FIG. 16. Comparison of LBM results and exact solution for the dimensionless temperature field of ϕ at $Pe = 10$.

Furthermore, Figs. 18 and 19 present the interfacial scalars and fluxes (run on a 256×256 LBM grid), respectively, with simulation parameters $Pe = 10, H_2 = 0.5\delta x, \sigma = 3.5k_{31}$, $\tau_1 = 0.57$, and $\tau_3 = 0.52$. Three specific cases with varying thermal conductivity ratios were tested: *Case 1*: $k_{31} = 1$, *Case 2*: $k_{31} = 0.01$, and *Case 3*: $k_{31} = 100$. Again, to further elucidate the comparison of two proposed interface schemes in Sec. V C (denoted by "LBM,NF" for nonuniform tangential flux) and its simplified version in Sec. V A (denoted by "LBM,CF" for constant tangential flux), both are plotted in the scalar and flux plots in Figs. 18 and 19. It is apparent that the LBM solutions with the general scheme in Sec. V C implemented matches very well with the exact solution, while some noticeable discrepancy is observed for the solutions obtained with the "constant tangential flux" scheme. This is innately due to the nature of both schemes, with the general scheme in Sec. V C being able to account for the tangential flux variation.

Furthermore, to verify the order of accuracy of the evaluated interfacial scalar and flux values when using the general interface scheme in Sec. V C, the L_2-norm errors E_{2_tint} and E_{2_qint} defined in Eqs. (53), (54) are computed and presented in Figs. 20 and 21, respectively.

From the results shown, first-order convergence is observed for all cases for E_{2_tint}, and second-order convergence for E_{2_qint}, with an increase in error magnitude as H_2 is increased. The higher convergence order of the interfacial flux is similar to that presented in Figs. 13 and 14. As expected, the degradation in the order of accuracy can be attributed to the addition of nonminuscule tangential heat flux along the sandwiched layer interfaces and the associated interpolation of the q_l and q_r components used to construct the general interface scheme. Nonetheless, the proposed schemes in this work show considerable promise with low error magnitude and the benefit with greatly reduced computational demand compared to a typical computational setup of including LB nodes in all domains.

VII. CONCLUSIONS

In this paper, a computationally efficient interface treatment within the lattice Boltzmann method framework was proposed to resolve the conjugate conditions that are evident on opposing sides of a thin layer of material bound by separate and distinct domains of interest. The proposed treatment is attractive as it satisfies the conjugate conditions on both sides and avoids fine meshing and computation within the thin layer. Three particular interface schemes were developed, presented in Secs. V A through V C. In Sec. V A, the scheme was presented for planar coordinates specifically for cases with zero or constant heat flux tangential to the thin-layer interface. Section V B thus presents a similar analysis for cylindrical coordinates. Finally, Sec. V C presents a general interface scheme with flux correction that is applicable to a wider range of applications involving conjugate heat transfer across thin layers without any constraint on the tangential flux variation.

A detailed order of accuracy analysis was then presented for three representative benchmark cases. The quantities investigated include the interior temperature fields as well as

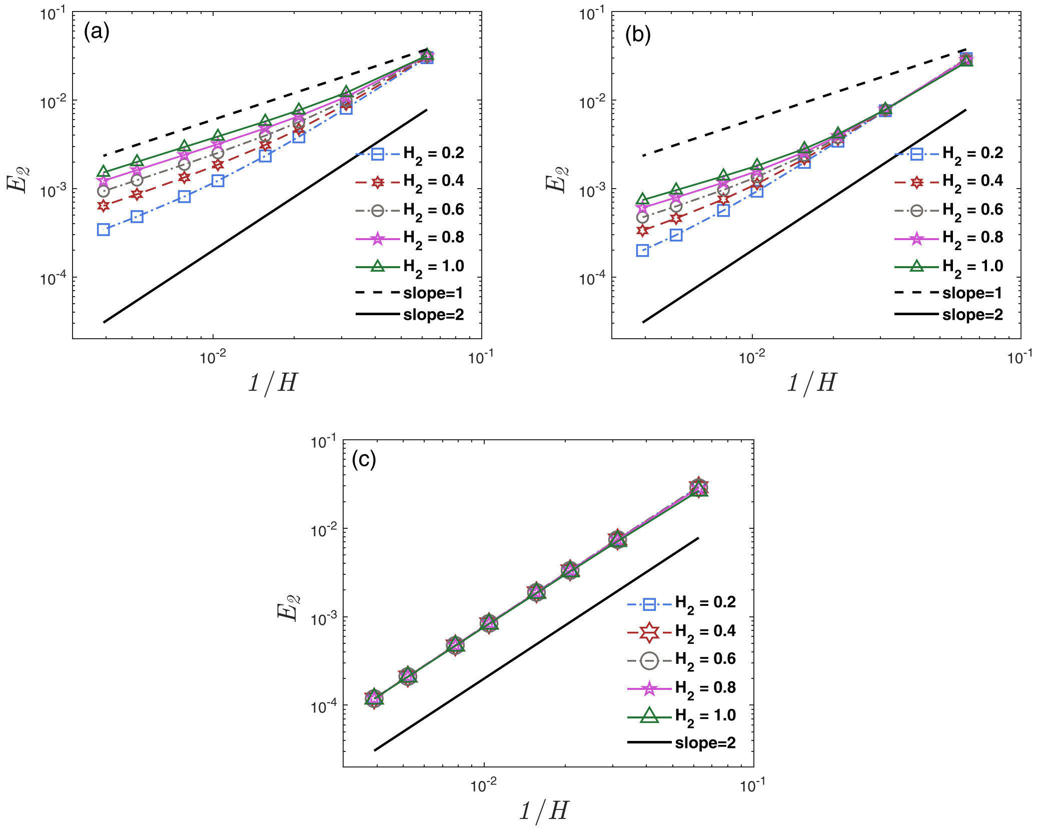

FIG. 17. L_2-norm errors for the interior temperature field, E_2, at varied H_2 and $Pe = 20$ vs the grid resolution, $1/H$, for different interface schemes (a) neglecting tangential fluxes as in Sec. V A, (b) general scheme in Sec. V C, and (c) general scheme in Sec. V C but with exact tangential fluxes used.

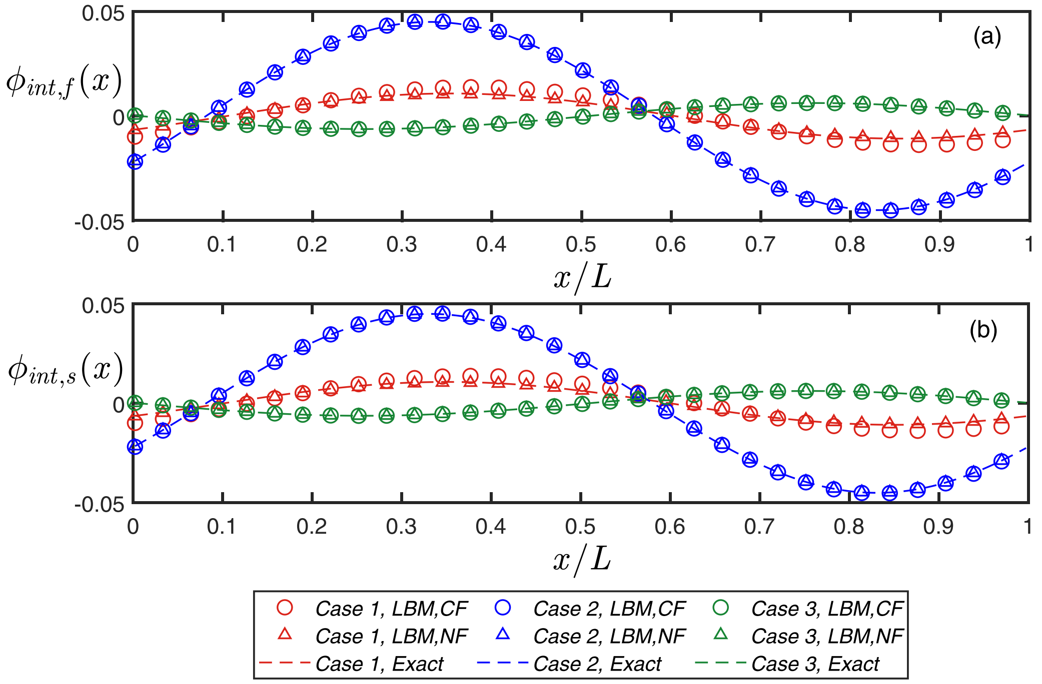

FIG. 18. Profiles of the interfacial scalar ϕ_{int} at (a) $y = H_1$ and (b) $y = H_1 + H_2$ for $\tau_1 = \tau_3 = 0.55$ at $Pe = 10$.

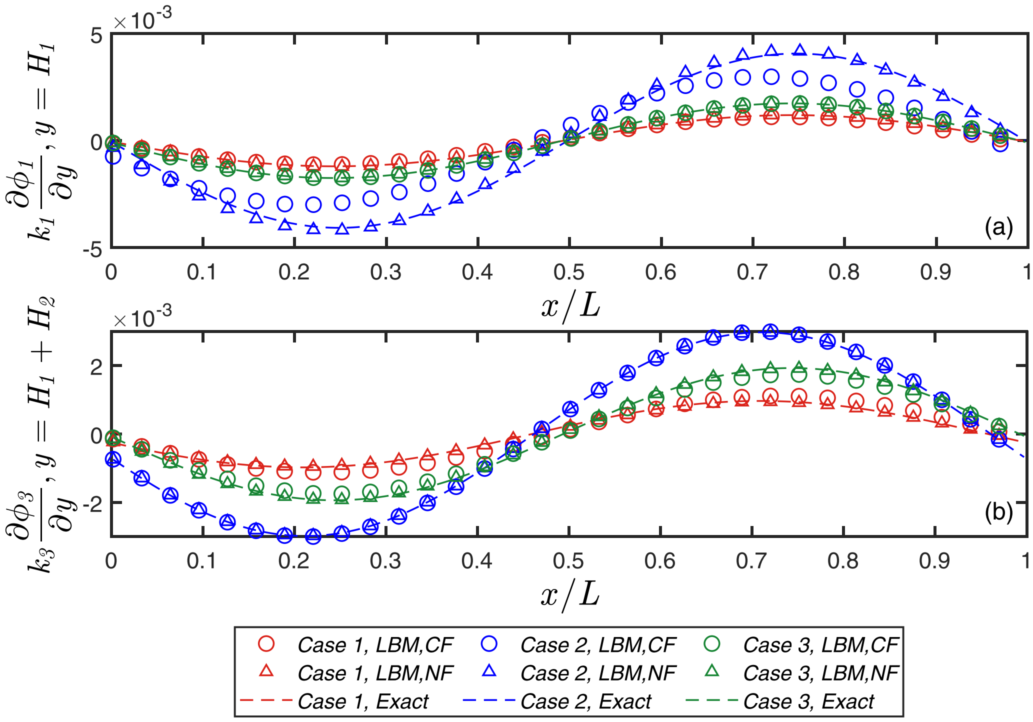

FIG. 19. Profiles of the interfacial flux $(k\partial\phi/\partial y)_{\text{int}}$ at (a) $y = H_1$ and (b) $y = H_1 + H_2$ for $\tau_1 = \tau_3 = 0.55$ at $Pe = 10$.

the evaluated interfacial temperatures and fluxes. The first two cases have no flux variation in the tangential direction; thus, the proposed schemes are able to preserve the intrinsic second-order accuracy of the LB model. The final test case shows the advantage of the correction scheme and it was verified that the proposed scheme is first-order accurate for general cases. Overall, the demonstrated results show the validity of the proposed interface treatment, which shows a strong propensity for numerical solvers with a focus on improved computational efficiency with retainment of a high degree of accuracy.

ACKNOWLEDGMENT

This material is based upon work supported by the U.S. Department of Energy's Office of Energy Efficiency and Renewable Energy (EERE) under the Solar Energy Technologies Office (SETO) Award No. DE-EE0008992.

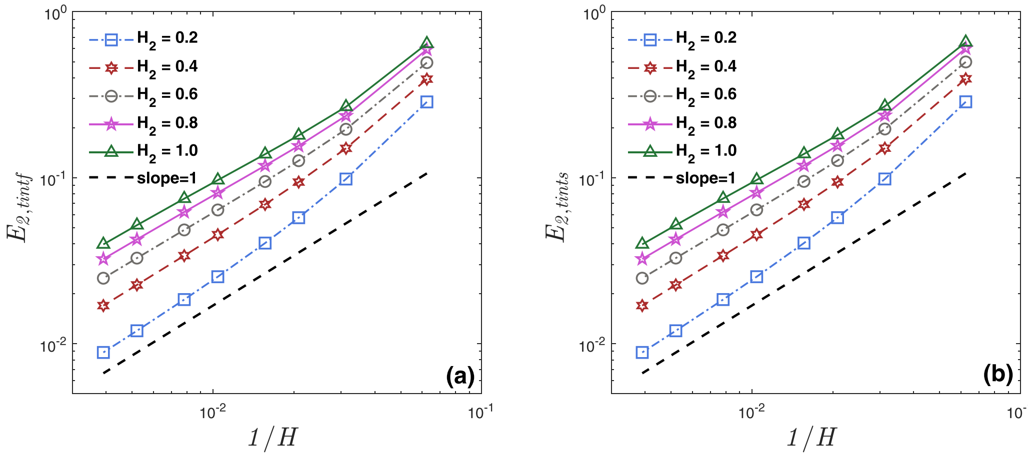

FIG. 20. L_2-norm errors for the interfacial scalar values (a) ϕ_{intf} at $y = H_1$ and (b) ϕ_{ints} at $y = H_1 + H_2$ versus the grid resolution with the general interface scheme in Sec. V C. Simulation parameters include $Pe = 20$, $k_{31} = 2/3$, $k_{23} = 15$, $\sigma = 2/3$, $\tau_1 = 0.60$, $\tau_3 = 0.60$.

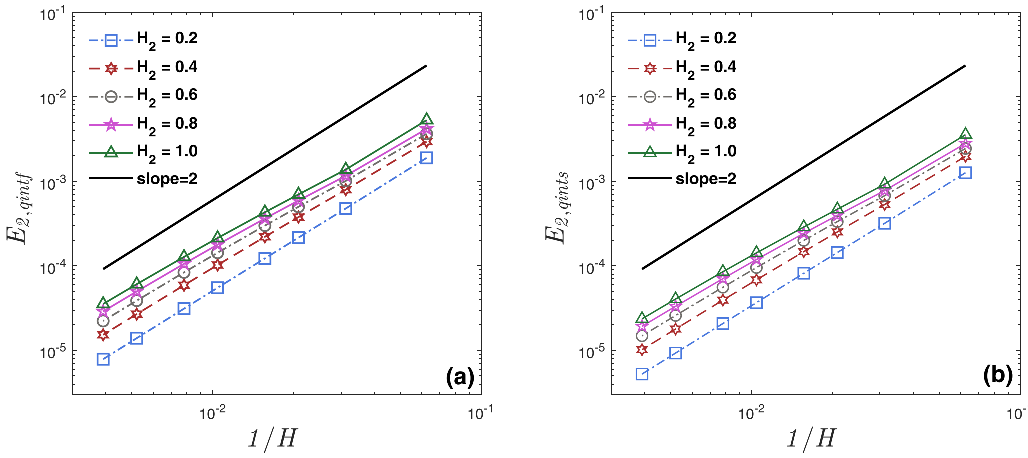

FIG. 21. L_2-norm errors for the interfacial fluxes in the normal direction (a) q_{intf} at $y = H_1$ and (b) q_{ints} at $y = H_1 + H_2$ vs the grid resolution with the general interface scheme in Sec. V C with the same simulation parameters as in Fig. 20.

APPENDIX: ANALYTICAL SOLUTIONS TO THE TEST CASES IN SECS. VI A AND VI C

For diffusion within the three-layered domain in Fig. 5, the governing CDEs are written as

$$\frac{\partial}{\partial y}\left(k_1\frac{\partial\phi_1}{\partial y}\right) + k_1 S(y) = 0, \quad 0 \leqslant y < H_1, \tag{A1a}$$

$$\frac{\partial}{\partial y}\left(k_2\frac{\partial\phi_2}{\partial y}\right) + k_2 S(y) = 0, \quad H_1 \leqslant y < H_1 + H_2, \tag{A1b}$$

$$\frac{\partial}{\partial y}\left(k_3\frac{\partial\phi_3}{\partial y}\right) + k_3 S(y) = 0, \quad H_1 + H_2 \leqslant y \leqslant H = (H_1 + H_2 + H_3), \tag{A1c}$$

with

$$S(y) = \left[\frac{12a}{H^2}\left(\frac{y}{H}\right)^2 + \frac{6b}{H^2}\left(\frac{y}{H}\right) + \frac{2c}{H^2}\right], \quad 0 \leqslant y < H_1, \tag{A2a}$$

$$S(y) = 0, \quad H_1 \leqslant y < H_1 + H_2, \tag{A2b}$$

$$S(y) = \left[\frac{12a}{H^2}\left(\frac{y}{H}\right)^2 + \frac{6b}{H^2}\left(\frac{y}{H}\right) + \frac{2c}{H^2}\right], \quad H_1 + H_2 \leqslant y \leqslant H. \tag{A2c}$$

With standard conjugate conditions at the two interfaces, the exact solutions for the thermal field can be expressed as

$$\phi_1(y) = -\left[\frac{a}{H^4}y^4 + \frac{b}{H^3}y^3 + \frac{c}{H^2}y^2\right] + C_1 y, \tag{A3a}$$

$$\phi_2(y) = C_2 y + C_4, \tag{A3b}$$

$$\phi_3(y) = -\left[\frac{a}{H^4}y^4 + \frac{b}{H^3}y^3 + \frac{c}{H^2}y^2\right] + C_3 y + C_5, \tag{A3c}$$

where

$$C_1 = \frac{\eta_1 + \eta_2 + \eta_3 + \eta_4\left(\frac{H_2}{k_2} + \frac{H_3}{k_3}\right) + \eta_5\left(\frac{H_3}{k_3}\right)}{H_1 + \frac{k_1}{k_2}H_2 + \frac{k_1}{k_3}H_3} \tag{A4a}$$

$$C_2 = \frac{k_1 C_1 - \eta_4}{k_2}, \quad C_3 = \frac{k_1 C_1 - \eta_4 - \eta_5}{k_3}, \tag{A4b}$$

$$C_4 = H_1 C_1 - \frac{k_1}{k_2}(H_1 C_1) + \frac{H_1\eta_4}{k_2} - \eta_2, \quad C_5 = \eta_1 - \frac{H}{3}(k_1 C_1 - \eta_4 - \eta_5), \tag{A4c}$$

$$\eta_1 = 1 + a + b + c, \quad \eta_2 = \frac{a}{H^4}{H_1}^4 + \frac{b}{H^3}{H_1}^3 + \frac{c}{H^2}{H_1}^2, \tag{A4d}$$

$$\eta_3 = -\frac{a}{H^4}(H_1 + H_2)^4 - \frac{b}{H^3}(H_1 + H_2)^3 - \frac{c}{H^2}(H_1 + H_2)^2, \tag{A4e}$$

$$\eta_4 = k_1\left[\frac{4a}{H^4}{H_1}^3 + \frac{3b}{H^3}{H_1}^2 + \frac{2c}{H^2}H_1\right], \tag{A4f}$$

$$\eta_5 = -k_3\left[\frac{4a}{H^4}(H_1+H_2)^3 + \frac{3b}{H^3}(H_1+H_2)^2 + \frac{2c}{H^2}(H_1+H_2)\right]. \tag{A4g}$$

For convection-diffusion within the channel with the three-layered domain in Fig. 13, the governing CDEs are

$$U\frac{\partial\phi_1}{\partial x} = D_1\left(\frac{\partial^2\phi_1}{\partial x^2} + \frac{\partial^2\phi_1}{\partial y^2}\right) \quad \text{for} \quad 0 \leqslant y < H_1, \tag{A5a}$$

$$0 = D_2\left(\frac{\partial^2\phi_2}{\partial x^2} + \frac{\partial^2\phi_2}{\partial y^2}\right) \quad \text{for} \quad H_1 \leqslant y < H_1 + H_2, \tag{A5b}$$

$$U\frac{\partial\phi_3}{\partial x} = D_3\left(\frac{\partial^2\phi_3}{\partial x^2} + \frac{\partial^2\phi_3}{\partial y^2}\right) \quad \text{for} \quad H_1 + H_2 \leqslant y < H = (H_1 + H_2 + H_3). \tag{A5c}$$

Also with standard conjugate conditions at the two interfaces, the exact solution for the thermal domain can be solved as

$$\phi_{\text{ex},1}(x,y) = \text{Re}\{e^{ikx}[C_3e^{\lambda_1 y} + (1-C_3)e^{-\lambda_1 y}]\}, \tag{A6a}$$

$$\phi_{\text{ex},2}(x,y) = \text{Re}\{e^{ikx}[C_2e^{\lambda_2 y} + C_1e^{-\lambda_2 y}]\}, \tag{A6b}$$

$$\phi_{\text{ex},3}(x,y) = \text{Re}\left\{e^{ikx}\left[\left(a_5 - {a_5}^2C_4\right)e^{\lambda_3 y} + C_4e^{-\lambda_3 y}\right]\right\}, \tag{A6c}$$

where "Re" denotes the real part of a complex number, and the coefficients are

$$\lambda_{1,2,3} = k\sqrt{1 + \frac{iU_{1,2,3}}{D_{1,2,3}k}}, \quad k = 2\pi/L, \tag{A7a}$$

$$a_1 = e^{-\lambda_1 H_1}, \quad a_2 = e^{-\lambda_2 H_1}, \quad a_3 = e^{-\lambda_2(H_1+H_2)}, \quad a_4 = e^{-\lambda_3(H_1+H_2)}, \quad a_5 = e^{-\lambda_3 H}, \tag{A7b}$$

$$b_1 = \frac{a_1}{a_2 - {a_1}^2a_2}, \quad b_2 = \frac{a_1{a_2}^2}{a_2 - {a_1}^2a_2}, \quad b_3 = -\frac{{a_1}^2a_2}{a_2 - {a_1}^2a_2}, \tag{A7c}$$

$$b_4 = \frac{k_2\lambda_2a_1}{k_1\lambda_1\left(a_2 + {a_1}^2a_2\right)}, \quad b_5 = -\frac{k_2\lambda_2a_1{a_2}^2}{k_1\lambda_1\left(a_2 + {a_1}^2a_2\right)}, \quad b_6 = \frac{{a_1}^2a_2}{a_2 + {a_1}^2a_2}, \tag{A7d}$$

$$d_1 = \frac{a_4}{a_3{a_4}^2 - a_3{a_5}^2}, \quad d_2 = \frac{{a_3}^2a_4}{a_3{a_4}^2 - a_3{a_5}^2}, \quad d_3 = -\frac{a_3a_5}{a_3{a_4}^2 - a_3{a_5}^2}, \tag{A7e}$$

$$d_4 = \frac{k_2\lambda_2a_4}{k_3\lambda_3\left(-a_3{a_5}^2 - a_3{a_4}^2\right)}, \quad d_5 = -\frac{k_2\lambda_2{a_3}^2a_4}{k_3\lambda_3\left(-a_3{a_5}^2 - a_3{a_4}^2\right)}, \quad d_6 = -\frac{a_3a_5}{\left(-a_3{a_5}^2 - a_3{a_4}^2\right)}, \tag{A7f}$$

$$C_1 = \frac{\left(\frac{d_6-d_3}{d_1-d_4}\right) - \left(\frac{b_6-b_3}{b_1-b_4}\right)}{\left(\frac{b_5-b_2}{b_1-b_4}\right) - \left(\frac{d_5-d_2}{d_1-d_4}\right)}, \quad C_2 = \frac{C_1(b_5-b_2) + b_6 - b_3}{b_1 - b_4}, \tag{A7g}$$

$$C_3 = \frac{k_2\lambda_2(a_1C_2 - a_1{a_2}^2C_1) + {a_1}^2a_2}{k_1\lambda_1(a_2 + {a_1}^2a_2)}, \quad C_4 = \frac{a_4C_2 + {a_3}^2a_4C_1 - a_3a_5}{a_3{a_4}^2 - a_3{a_5}^2}. \tag{A7h}$$

---

[1] J.-M. Yin, Q.-Y. Zheng, and X.-R. Zhang, Heat transfer model of a particle energy storage-based moving packed bed heat exchanger, Energy Storage **2**, e113 (2020).

[2] K. J. Albrecht and C. K. Ho, Design and operating considerations for a shell-and-plate, moving packed-bed, particle-to-SCO2 heat exchanger, Sol. Energy **178**, 331 (2019).

[3] J. A. W. Gut and J. M. Pinto, Modeling of plate heat exchangers with generalized configurations, Int. J. Heat Mass Transfer **46**, 2571 (2003).

[4] W. Lipiński, E. Abbasi-Shavazi, J. Chen, J. Coventry, M. Hangi, S. Iyer, A. Kumar, L. Li, S. Li, J. Pye, J. F. Torres, B. Wang, Y. Wang, and V. M. Wheeler, Progress in heat transfer research for high-temperature solar thermal applications, Appl. Therm. Eng. **148**, 116137 (2020).

[5] Y. Zhao, C. Y. Zhao, C. N. Markides, H. Wang, and W. Li, Medium- and high-temperature latent and thermochemical heat storage using metals and metallic compounds as heat storage media: A technical review, Appl. Energy **280**, 115950 (2020).

[6] L. Li, C. Chen, A. Singh, N. Rahmatian, N. AuYeung, K. Randhir, R. Mei, J. F. Klausner, D. W. Hahn, and J. Petrasch, A transient heat transfer model for high temperature solar thermochemical reactors, Int. J. Hydrogen Energy **41**, 2307 (2016).

[7] S. B. Riffat, X. Zhao, and P. S. Doherty, Developing a theoretical model to investigate thermal performance of a thin

membrane heat-pipe solar collector, Appl. Therm. Eng. **25**, 899 (2005).
[8] L. M. Sun, N. Ben Amar, and F. Meunier, Numerical study on coupled heat and mass transfers in an absorber with external fluid heating, Heat Recover. Syst. CHP **15**, 19 (1995).
[9] M. Duquesne, J. Toutain, A. Sempey, S. Ginestet, and E. Palomo Del Barrio, Modeling of a nonlinear thermochemical energy storage by adsorption on zeolites, Appl. Therm. Eng. **71**, 469 (2014).
[10] K. Ndiaye, S. Ginestet, and M. Cyr, Modelling and experimental study of low temperature energy storage reactor using cementitious material, Appl. Therm. Eng. **110**, 601 (2017).
[11] E. Rezaei, M. Barbato, A. Ortona, and S. Haussener, Design and optimization of a high-temperature latent heat storage unit, Appl. Energy **261**, 114330 (2020).
[12] Y. Wang and K. Vafai, An experimental investigation of the thermal performance of an asymmetrical flat plate heat pipe, Int. J. Heat Mass Transfer **43**, 3753 (2000).
[13] Y. Başoğul, C. Demircan, and A. Keçebaş, Determination of optimum insulation thickness for environmental impact reduction of pipe insulation, Appl. Therm. Eng. **101**, 121 (2016).
[14] L. Vander Tempel, W. Potze, and J. H. Lammers, Transient heat conduction in a thin layer between semi-infinite media in polymer shaping, J. Heat Transfer **140**, 041301 (2018).
[15] H. Yoshida and M. Nagaoka, Multiple-relaxation-time lattice Boltzmann model for the convection and anisotropic diffusion equation, J. Comput. Phys. **229**, 7774 (2010).
[16] Z. Chai and B. Shi, Multiple-relaxation-time lattice Boltzmann method for the Navier-Stokes and nonlinear convection-diffusion equations: Modeling, analysis, and elements, Phys. Rev. E **102**, 023306 (2020).
[17] I. Ginzburg, Steady-state two-relaxation-time lattice Boltzmann formulation for transport and flow, closed with the compact multi-reflection boundary and interface-conjugate schemes, J. Comput. Sci. 101215 (2020).
[18] L. Li, R. Mei, and J. F. Klausner, Lattice Boltzmann models for the convection-diffusion equation: D2Q5 vs D2Q9, Int. J. Heat Mass Transfer **108**, 41 (2017).
[19] L. Li, R. Mei, and J. F. Klausner, Boundary conditions for thermal lattice Boltzmann equation method, J. Comput. Phys. **237**, 366 (2013).
[20] T. Zhang, B. Shi, Z. Guo, Z. Chai, and J. Lu, Erratum: General bounce-back scheme for concentration boundary condition in the lattice-Boltzmann method [Phys. Rev. E 85, 016701 (2012)], Phys. Rev. E **88**, 029903(E) (2013).
[21] I. Ginzburg, Generic boundary conditions for lattice Boltzmann models and their application to advection and anisotropic dispersion equations, Adv. Water Resour. **28**, 1196 (2005).
[22] L. Li, C. Chen, R. Mei, and J. F. Klausner, Conjugate heat and mass transfer in the lattice boltzmann equation method, Phys. Rev. E **89**, 043308 (2014).
[23] Z. Hu, J. Huang, and W. A. Yong, Lattice Boltzmann method for convection-diffusion equations with general interfacial conditions, Phys. Rev. E **93**, 043320 (2016).
[24] Y. T. Mu, Z. L. Gu, P. He, and W. Q. Tao, Lattice Boltzmann method for conjugated heat and mass transfer with general interfacial conditions, Phys. Rev. E **98**, 043309 (2018).
[25] K. Guo, L. Li, G. Xiao, N. Auyeung, and R. Mei, Lattice Boltzmann method for conjugate heat and mass transfer with interfacial jump conditions, Int. J. Heat Mass Transfer **88**, 306 (2015).
[26] L. Li, Multiple-time-scaling lattice Boltzmann method for the convection diffusion equation, Phys. Rev. E **99**, 063301 (2019).
[27] D. Korba, N. Wang, and L. Li, Accuracy of interface schemes for conjugate heat and mass transfer in the lattice Boltzmann method, Int. J. Heat Mass Transfer **156**, 119694 (2020).
[28] O. Filippova and D. Hänel, Grid refinement for lattice-BGK models, J. Comput. Phys. **147**, 219 (1998).
[29] D. Yu, R. Mei, and W. Shyy, A multi-block lattice Boltzmann method for viscous fluid flows, Int. J. Numer. Methods Fluids **39**, 99 (2002).
[30] D. Lagrava, O. Malaspinas, J. Latt, and B. Chopard, Advances in multi-domain lattice Boltzmann grid refinement, J. Comput. Phys. **231**, 4808 (2012).
[31] R. Huang and H. Wu, Multiblock approach for the passive scalar thermal lattice Boltzmann method, Phys. Rev. E **89**, 043303 (2014).
[32] W.-Z. Fang, J.-J. Gou, L. Chen, and W.-Q. Tao, A multi-block lattice Boltzmann method for the thermal contact resistance at the interface of two solids, Appl. Therm. Eng. **138**, 122 (2018).
[33] H. Yoshida and M. Nagaoka, Lattice Boltzmann method for the convection-diffusion equation in curvilinear coordinate systems, J. Comput. Phys. **257**, 884 (2014).
[34] H. Chen, S. Chen, and W. H. Matthaeus, Recovery of the Navier-Stokes equations using a lattice-gas Boltzmann method, Phys. Rev. A **45**, R5339 (1992).
[35] I. Ginzburg, Equilibrium-type and link-type lattice Boltzmann models for generic advection and anisotropic-dispersion equation, Adv. Water Res. **28**, 1171 (2005).
[36] M. Espinoza-Andaluz, A. Moyón, and M. Andersson, A comparative study between D2Q9 and D2Q5 lattice Boltzmann scheme for mass transport phenomena in porous media, Comput. Math. Appl. **78**, 2886 (2019).
[37] L. Li, R. Mei, and J. F. Klausner, Multiple-relaxation-time lattice Boltzmann model for the axisymmetric convection diffusion equation, Int. J. Heat Mass Transfer **67**, 338 (2013).
[38] L. Zhang, S. Yang, Z. Zeng, J. Chen, L. Wang, and J. W. Chew, A comparative study of the axisymmetric lattice Boltzmann models under the incompressible limit, Comput. Math. Appl. **74**, 817 (2017).
[39] Z. Wang, J. Zhang, and W. Zhang, Lattice Boltzmann simulations of axisymmetric natural convection with anisotropic thermal diffusion, Int. J. Heat Mass Transfer **101**, 1304 (2016).
[40] J. G. Zhou, Axisymmetric lattice Boltzmann method, Phys. Rev. E **78**, 036701 (2008).
[41] H. Huang and X. Y. Lu, Theoretical and numerical study of axisymmetric lattice Boltzmann models, Phys. Rev. E **80**, 016701 (2009).
[42] L. Li, R. Mei, and J. F. Klausner, Heat transfer evaluation on curved boundaries in thermal lattice Boltzmann equation method, J. Heat Transfer **136**, 012403 (2014).
[43] Z. Chai and T. S. Zhao, Nonequilibrium scheme for computing the flux of the convection-diffusion equation in the framework of the lattice Boltzmann method, Phys. Rev. E **90**, 013305 (2014).
[44] N. Wang, I. Kaur, P. Singh, and L. Li, Prediction of effective thermal conductivity of porous lattice structures and validation with additively manufactured metal foams, Appl. Therm. Eng. **187**, 116558 (2021).